Impacts of farmland decontamination on 137Cs transfers in rivers after Fukushima nuclear accident: Evidence from a retrospective sediment core study

Thomas Chalaux Clergue, Anthony Foucher, Pierre-Alexis Chaboche, Seiji Hayashi, Hideki Tsuji, Yoshifumi Wakiyama, Sylvain Huon, Rosalie Vandromme, Olivier Cerdan, Atsushi Nakao, et al.

Science of the Total Environment 947 (2024) 174546

Contents lists available at ScienceDirect

Science of the Total Environment

journal homepage: www.elsevier.com/locate/scitotenv

Impacts of farmland decontamination on ^{137}Cs transfers in rivers after Fukushima nuclear accident: Evidence from a retrospective sediment core study

Thomas Chalaux-Clergue [a,*], Anthony Foucher [a], Pierre-Alexis Chaboche [b,c], Seiji Hayashi [d], Hideki Tsuji [d], Yoshifumi Wakiyama [c], Sylvain Huon [e], Rosalie Vandromme [f], Olivier Cerdan [f], Atsushi Nakao [g], Olivier Evrard [a,*]

[a] Laboratoire des Sciences du Climat et de l'Environnement (LSCE-IPSL), Université Paris-Saclay, UMR 8212 (CEA-CNRS-UVSQ), Gif-sur-Yvette 91190, France
[b] International Research Fellow of Japan Society for the Promotion of Science, Postdoctoral Fellowships for Research in Japan (Standard), Japan
[c] Institute of Environmental Radioactivity (IER), University of Fukushima, Fukushima, Japan
[d] National Institute for Environmental Science (NIES), Fukushima Branch, 10-2 Fukasaku, Miharu, Tamura, Fukushima 963-7700, Japan
[e] Sorbonne Universités UPMC Université Paris 06, Institut d'Ecologie et des Sciences de l'Environnement de Paris (iEES), case 120, 4 place Jussieu, Paris cedex 05 75252, France
[f] Risk and Prevention Division, Bureau de Recherches Géologiques et Minières (BRGM), Orléans F-45060, France
[g] Graduate School of Life and Environmental Sciences, Kyoto Prefectural University, Shimogamo, Hangi, Sakyo-ku, Kyoto 606-8522, Japan

HIGHLIGHTS

- A sediment core draining a Fukushima fallout-affected catchment was analysed.
- Farmland decontamination impact on particle-bound ^{137}Cs transfer was reconstructed.
- Sediment origin was determined using sediment source fingerprinting techniques.
- Forests act as a stable and long-term source of ^{137}Cs-contaminated sediment.
- Farmland decontamination and 5-years abandonment resulted in equivalent ^{137}Cs fluxes.

GRAPHICAL ABSTRACT

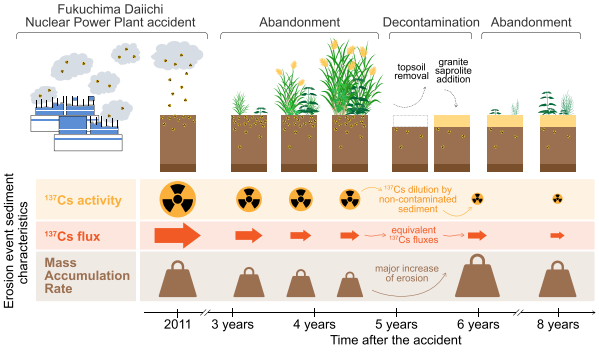

ARTICLE INFO

Editor: Ashantha Goonetilleke

Keywords:
Soil erosion
Environmental pollution
Radiocesium transfer
Source-to-sink

ABSTRACT

Following the Fukushima Daiichi Nuclear Power Plant disaster in March 2011, the Japanese government initiated an unprecedented decontamination programme to remediate ^{137}Cs-contaminated soils and allow population return. This programme involved the removal of topsoil under farmland and residential land, and its replacement with "fresh soil" composed of granitic saprolite. However, decontamination was limited to these two land uses, without remediating forests, which cover 70 % of the surface area in the affected region. In this unprecedented context, the specific impact of this unique decontamination programme on ^{137}Cs transfers in river systems remains to be quantified at the catchment scale. In this study, based on the analysis of a sediment core collected in

* Corresponding authors.
E-mail addresses: thomaschalaux@icloud.com (T. Chalaux-Clergue), olivier.evrard@lsce.ipsl.fr (O. Evrard).

https://doi.org/10.1016/j.scitotenv.2024.174546
Received 19 March 2024; Received in revised form 3 July 2024; Accepted 4 July 2024
Available online 9 July 2024

Sediment source fingerprinting
Soil remediation

June 2021 in the Mano Dam reservoir draining a decontaminated catchment, the effects of soil decontamination on particle-bound ^{137}Cs dynamics and sediment source contributions in response to a succession of extreme precipitation events were retrospectively assessed. The sequence of sediment layer deposition and its chronology were reconstructed through the analysis of several diagnostic properties (organic matter, elemental geochemistry, visible colourimetry, granulometry) and contextual information. During abandonment (2011–2016), cropland contribution decreased (31 %). Concurrently, ^{137}Cs activity and deposition flux decreased (19 and 29 % $year^{-1}$, respectively). Following decontamination (2017), sediment transfer increased (270 %) in response to increased contributions from decontaminated cropland and "fresh soil" (625 % and 180 % respectively). Meanwhile, forest contributions remained stable. In contrast, ^{137}Cs activity dropped (65 %), although ^{137}Cs deposition flux remained constant. Forests acted as a stable source of ^{137}Cs. Accordingly, ^{137}Cs deposition flux after decontamination (2016–2021) was similar to that observed during the 5-years period of land abandonment (2011–2016), as a result of the regrowth of spontaneous vegetation over farmland, protecting soil against erosion. Future research should further investigate the impact of longer land abandonment that prevailed in some regions decontaminated lately on the ^{137}Cs fluxes in the rivers.

1. Introduction

The nuclear accident at the Fukushima Daiichi Nuclear Power Plant (FDNPP) that occurred in March 2011 released a substantial amount of radionuclides into the environment (Morino et al., 2013), of which about 20 % deposited over continental land (Onda et al., 2020). Of all the radionuclides released, ^{137}Cs is particularly problematic in terms of short and long term environmental and human health impacts due to its relatively long half-life ($T_{1/2}$) of 30 *years* and the large amounts of this substance that were released, with about 13 *PBq* (Chino et al., 2011; Kobayashi et al., 2013; Steinhauser, 2014). Most of the ^{137}Cs that deposited onto terrestrial environments (2.7 *PBq*) has accumulated in the Fukushima Prefecture (2.0 *PBq*) (Kato et al., 2019; Taniguchi et al., 2019). About 83 % of the surface area in this Prefecture (i.e. $11,430\ km^2$) has received at least 5 $kBq\ m^{-2}$, and 26 % (i.e. $3,520\ km^2$) has received at least 100 $kBq\ m^{-2}$ (Kato et al., 2019). The inhabitants living within a 20-km radius around FDNPP (Evacuation Zone) and those who were exposed to a radioactive dose rate exceeding 20 $mSv\ yr^{-1}$ in 2011 (Planned Evacuation Zone) were evacuated in priority. A total of eleven municipalities, with a population of about 80,000 people and covering an area of $1,150\ km^2$, were under an evacuation order and classified as Residence Restriction Area. According to the decontamination programme, these municipalities were then classified as Special Decontamination Zone (SDZ) or Difficult-to-Return Zone (DTRZ) depending on local ambient dose rates (MoE, 2018; Taniguchi et al., 2019; Evrard et al., 2019b).

Once deposited onto the ground, ^{137}Cs is strongly and quasi-permanently bound to fine soil particles such as silt and clay (Sawhney, 1972; He and Walling, 1996), which has been confirmed in Fukushima Prefecture soils (Saito et al., 2014; Nakao et al., 2014, 2015). Consequently, 90–99 % of fallout radiocesium was found to be accumulated in the uppermost 5 *cm* of undisturbed soils (Kato et al., 2012; Lepage et al., 2015). In addition, in relation to ^{137}Cs behaviour in soil, the transfer from soil to plant was found to be limited in annual or perennial herbs and trees (Yamashita et al., 2014; Tamaoki et al., 2016; Onda et al., 2020), so that the nearly all of ^{137}Cs deposited onto the ground remained in the soil. Within the Fukushima Prefecture, 74 % of the ^{137}Cs deposition occurred over forests and 19 % over farmland (paddy fields and other farmland) (Kato et al., 2019). To enable a rapid return of the population and the resumption of agricultural activities, the Japanese government carried out extensive decontamination in farmland, urban areas and within a 20-*m* buffer zone in forests around residential areas and along roads (MoE, 2015; Evrard et al., 2020). In the SDZ, by March 2017, decontamination was conducted on 410 km^2 (36 % of the SDZ area), of which 21 % was under farmland (about 87 km^2) (MoE, 2023a, in Japanese).

In farmland, the decontamination procedure depended on the initial ^{137}Cs activity in soils (MoE, 2013, 2015, 2018). On the one hand, in soils with ^{137}Cs activities below 5 $kBq\ kg^{-1}$, inversion tillage of a layer of about 30 to 45 *cm* depth was carried out. On the other hand, in soils with activities exceeding 5 $kBq\ kg^{-1}$, decontamination consisted of four steps: (1) the removal of the upper 5 *cm* layer of soil, (2) the addition of a granite saprolite extracted from local quarries opened for this purpose to replace the removed soil ($55.5\ m^3$ per $1.000\ m^2$). The Japanese authorities refer to this material as "fresh soil". Then, to prepare the return of farmers, (3) soil fertility was restored with two types of amendments applied: (a) carbonate (as needed) and phosphorus silicate (about 0.8 $t\ ha^{-1}$) or (b) zeolite amendment (about 0.5 $t\ ha^{-1}$). Finally, the soil was (4) prepared for recultivation by mixing the saprolite layer and soil productivity recovery materials with the underlying residual soil layer through a double ploughing down to a depth of about 25 to 30 *cm*. Accordingly, decontamination comprised three main phrases: decontamination (step 1), remediation (step 2) and preparation for recultivation (steps 3 and 4).

Soil decontamination proved to be effective in reducing radioactive ambient air dose rates, from 20 to 70 % compared to the initial situation in 2011 (MoE, 2018; Onda et al., 2020), along with a decrease of individual exposure levels (Tsubokura et al., 2019). Soil decontamination in the Fukushima Prefecture (including residential areas, farmland, forest and roads) by March 2020 generated 6.7 million m^3 of removed soil (MoE, 2023b). In parallel to decontamination, a decrease of particle-bound ^{137}Cs transported by rivers was observed year after year and was attributed to physical decay, previous erosion and the progress of decontamination (Evrard et al., 2016; Osawa et al., 2018; Konoplev et al., 2018; Vandromme et al., 2023). Indeed, particulate-bound ^{137}Cs accounted for a large portion (82 to 99 %) of ^{137}Cs transfer by water erosion during rainfall events (Yamashiki et al., 2014; Sakaguchi et al., 2015; Iwagami et al., 2017; Osawa et al., 2018). The maximum of particulate-bound ^{137}Cs contribution was found in the fine material such as the silt-sized fraction (3-63 μm) (Sakaguchi et al., 2015). The primary sources of particle-bound ^{137}Cs were shown to be paddy fields, other farmland types and urban areas despite their low relative landscape cover (Chartin et al., 2013; Lepage et al., 2016; Taniguchi et al., 2019). This disproportionate contribution was related to their very strong hydro-sedimentary connectivity, especially for paddy fields and their irrigation/drainage systems that connect them directly to the river networks (Chartin et al., 2013). In addition, as decontamination left the soil uncovered by vegetation and included the spreading of non-aggregated fresh soil, decontamination exacerbated soil erodibility (Wakahara et al., 2014; Evrard et al., 2019a; Feng et al., 2022). Accordingly, an increase in soil erosion was observed in 2015 in the Niida and Mano River catchments, and contribution of sediment originating from subsoil or fresh soil sources strongly increased compared to what was observed in previous years. Evrard et al. (2019b) found that an increase in the relative sediment contribution from subsoil from about 20 to 50 % after decontamination. However, spontaneous vegetation regrowth following abandonment or after decontamination led to a

rapid recovery of the soil protection against erosion (Lal, 2001; Zuazo and Pleguezuelo, 2009), thereby reducing the contribution of farmland to sediment and particle bound-^{137}Cs transfers (Feng et al., 2022).

This soil protection by vegetation is particularly important, as tropical cyclones and typhoons were shown to generate heavy rainfall and extensive erosion each year all across Japan. Despite its location in Northern Japan less exposed to typhoons than southern regions, Fukushima Prefecture has been hit by at least one typhoon or tropical storm each year since the FDNPP accident (Laceby et al., 2016a; Evrard et al., 2020). These extreme events, which generate about 60 % of the annual rainfall and 86 % of the annual rainfall erosivity in the steep geomorphological context of the mountainous catchment of the Fukushima region (Laceby et al., 2016a) have been identified as the main driver of sediment and hence particle-bound ^{137}Cs transfer across basins (Kitamura et al., 2016; Chartin et al., 2017; Evrard et al., 2020). The timing of decontamination is therefore crucial, as typhoons may occur when soils are left bare for remediation and are therefore particularly exposed to erosion, which can lead to significant transfers of soil and particle-bound radiocesium.

However, the overall pluriannual impact of decontamination on the transfers of radiocesium in river systems remains uncertain, as nearly 70 % of the area of Fukushima Prefecture is covered by forests (Hashimoto et al., 2012) and have not been decontaminated, although they account for 74 % of ^{137}Cs deposition (Kato et al., 2019). They have also been shown to contribute a significant proportion of contaminated material to the river systems (Laceby et al., 2016b; Huon et al., 2018; Evrard et al., 2019a). In addition, these results showed that forests may provide a potential long-term source of particulate contaminated matter (Evrard et al., 2019b).

To reconstruct the long-term impact of major landscape changes on sediment transfer in catchments, sediment core collection and analysis provide an effective approach (Foucher et al., 2023). In reservoir dams located at the outlet of catchments and under steady-state conditions, when incoming and outgoing water volumes are monitored and managed to maintain a constant lake water level, grain size sorting and sediment deposition occur along the former river course (Wetzel, 2001). As the reservoir widens, downstream at the transition from a riverine to a lacustrine environment, the velocity of the water decreases, allowing suspended particles to settle down. In this lacustrine zone upstream of the dam, sediment deposition is similar to that of natural lakes. Away from the reservoir inlet, mainly fine particles settle down, resulting in homogeneous, continuous, and well-organised sediment deposits. In the area affected by the Fukushima accident, such a typical deposition pattern could be identified by the observation of a single well-defined radiocesium peak (Huon et al., 2018; Konoplev et al., 2022). However, during extreme precipitation events, dam operators proceed to water releases to prevent, to maintain or to restore water level in the reservoir. These changes in water discharge volumes could increase the velocity of the water flow within the reservoir, which affects the sediment deposition pattern. Resulting in further downstream transport and deposition of coarser particles further in the lacustrine zone and even limiting the efficiency of sediment trapping by the reservoir. Huon et al. (2018) identified this pattern within the Mano Dam reservoir by studying four sediment cores collected at up-, mid- and downstream locations. During extreme precipitation events, coarser particles that usually deposit in the upper part of the reservoir were observed in the midstream sediment core. Further downstream, slighter changes were observed compared to those observed midstream with slightly coarser particle size distribution (higher D50), likely due to the long extension of the reservoir. Furthermore, changes in the respective contributions from cropland, forest and subsoil as sources of sediment were estimated along the sediment cores. However, sampling of these sediment cores took place in November 2014, on the onset of decontamination activities in the area, initiated on June 2014.

In this study, a new sediment core sampled in the downstream part of the Mano Dam reservoir was examined. This reservoir drains an early decontaminated agricultural catchment in the Fukushima Prefecture. This sediment core was investigated to reconstruct for the first time the impact of decontamination on sediment and radiocesium transfers through the river system. A combination of analyses of Mano Dam reservoir sediment core properties and ancillary data were used to (i) identify and date the sequence of sedimentary deposits associated with the occurrence of extreme precipitation events during the 2011–2021 period. Based on this reconstruction, (ii) the temporal evolution of ^{137}Cs activity, ^{137}Cs deposition flux, and sedimentary sources among three potential sources were determined to quantify the impact of these unprecedented landscape changes. Results of the lessons learnt in Fukushima are then discussed to guide the implementation of land management in the event of a major widespread pollution event that may occur in the future.

2. Materials and methods

2.1. Study site

Mano Dam reservoir ($1.4\ km^2$; 37.68887–37.76166°N, 140.66671–140.84290°E), also known as Hayama Lake, is located in Fukushima Prefecture in Northeastern Japan (Tohoku Region). The catchment of Mano Dam reservoir $\left(67\ km^2\right)$ corresponds to the mountainous upper part of the Mano River drainage area, and its elevation ranges from 170 *m* to 694 *m* above sea level. It is a typical mountainous agricultural catchment of the eastern part of Fukushima Prefecture, mainly dominated by forests (90 %). Due to its steep topography, farmland (i.e. cropland, grassland and paddy fields - 7 %) is concentrated in the valley bottoms (Fig. 1.a). Farmland in general and paddy fields in particular are strongly connected to river networks through irrigation systems, which results in their high hydro-sedimentary connectivity with river networks Chartin et al. (2017). Built-up areas cover less than 1 % of the catchment surface area.

The catchment is located in a Dfa cold climate with no dry season and hot summer according to Köppen's climatic classification (Beck et al., 2018). The regional hydrological year runs from November to October (Laceby et al., 2016a; Whitaker et al., 2022). Over the last 30-years period (1991–2021), the mean annual temperature was $13.4 \pm 0.5^{\circ} C\, y^{-1}$ (standard deviation = SD), ranging on average from $-1.5 \pm 0.9^{\circ} C$ to $30.5 \pm 2.1^{\circ} C$ in January and August, respectively. Annual precipitation amounted to $1207 \pm 216\ mm\, y^{-1}$ (SD). Most of the precipitation occurs between June and October, corresponding to 60 % of the annual precipitation and 86 % of the rainfall erosivity (Laceby et al., 2016a). This period corresponds to the Japanese typhoon season, with a peak of intensity from July to September in Fukushima Prefecture. Daily precipitation and maximum hourly precipitation records from four stations (Fukushima City, Hippo, Iitate, and Soma) of the Automated Meteorological Data Acquisition System (AMeDAS) network located within less than 20 *km* from the catchment boundaries (Fig. 1), were downloaded from the Japan Meteorological Agency website (JMA, 2023, in Japanese). The downloaded records covered the period from 1 January 2006 to the date of the sediment core sampling (8 June 2021). To identify typhoons and tropical storms, tracks of all tropical cyclones from the Regional Specialized Meteorological Center (RSMC) Tokyo - Typhoon Center (RSMC, 2023, 2024) were compared with local precipitation data, to identify those events that generated more than 60 and 100 *mm* of daily precipitation (Evrard et al., 2014). In addition, suspended sediment concentrations recorded at two hydrological stations located upstream of the Mano Dam reservoir were used (Hayashi et al., 2023). Sediment concentrations were measured at the first station (37.738391°N, 140.803943°E; Fig. 1) at 5-*min* intervals from June 2014 to September 2016, and at the second station (37.733191°N, 140.807709°E; Fig. 1) at 10-*min* intervals from January 2017 to December 2019. Daily suspended sediment fluxes were calculated from

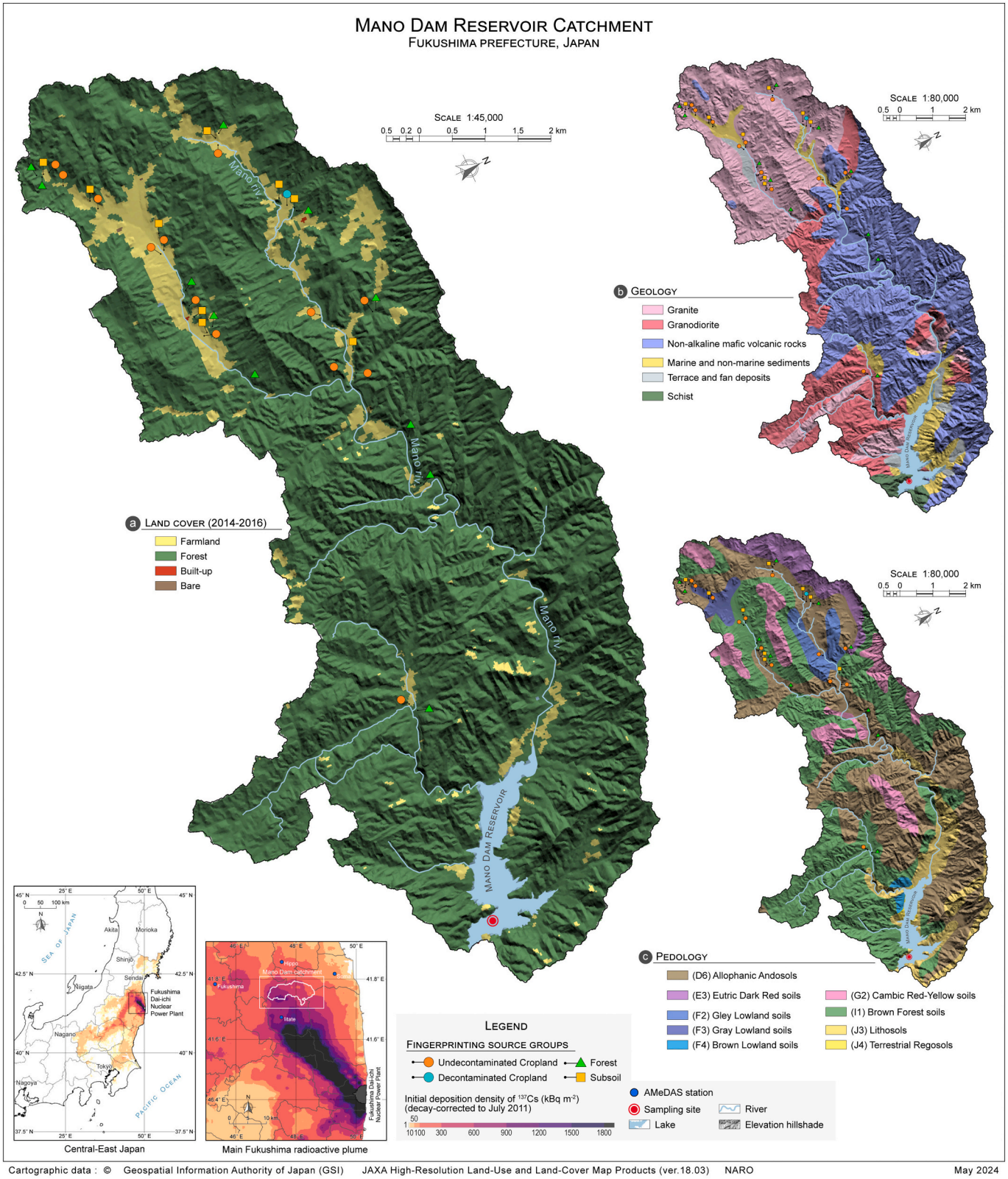

Fig. 1. Mano Dam reservoir catchment map of the main (a) land uses over the 2014–2016 period, (b) geological, and (c) pedological types with the location of source samples and sediment core sampling. Cartographic data from the Geospatial Information Authority of Japan (GSI), JAXA High-Resolution Land-Use and Lad-Cover Map Products (ver. 18.03), and NARO).

the instantaneous suspended sediment concentrations recorded by the hydrological stations.

In addition, the daily water level and discharge of the Mano Dam reservoir were downloaded from the Fukushima Prefecture website (Fukushima Prefecture, in Japanese). According to the hydroelectric plant operators, the water level of the dam was generally maintained below 176 *m*, which results in more water discharge during extreme precipitation events. These massive releases of water increase the flow of water within the reservoir, which limits the potential for suspended sediment to settle and therefore reduces the amount of sediment deposited within the reservoir.

The catchment is mainly underlied by plutonic rocks (48 % in total, with 31 % granite and 17 % granodiorite), non-alkaline mafic volcanic rocks (42 %) and some sedimentary rocks (9 % in total, with 7 % marine and non-marine sediments, < 1 % terrace and < 1 % fan deposits) and few schists (about 1 %) (Fig. 1.b). According to the Comprehensive Soil classification System of Japan (Obara et al. (2011, 2015), with the equivalence of soil types given according to the World Reference Base for Soil Resources (WRB)), the main soil types in the catchment are Brown Forest Soils (37 % - WRB: Cambisols/Stagnosols) and Allophanic Andosols (36 % - WRB: Silandic Andosols) and then Cambic Red-Yellow Soils (9 % - WRB: Cambisols) and Lithosols (9 % - WRB: Leptosols) (Fig. 1.c).

All maps and geographical processing were performed using the QGIS software (QGIS Development Team, 2022).

2.2. Catchment management after FDNPP accident

The Mano Dam reservoir catchment is located in the northern part of the Iitate village, which was evacuated in 2011 due to high exposure dose rates exceeding 20 *mSv* per year at that time, in relation with high ^{137}Cs activities in soils ranging from 80 to 1,200 $kBq\ m^{-2}$ (Kato et al., 2019). This part of the village of Iitate was submitted to a residential ban from 17 July 2012 to 31 March 2017 (MoE, 2023, in Japanese). Decontamination were carried out in the area from June 2014 to December 2016 (MoE, 2018). The daily progress of decontamination during this period was reconstructed using records of plot decontamination dates provided by the Japanese Ministry of the Environment (MoE). However, despite this evacuation order, the main land use proportions classified by satellite remained relatively stable during this period extended from 2006 to 2020 (JAXA, 2016, 2018, 2022), as the catchment is dominated by forest, and cropland was maintained during the evacuation to prevent the development of trees prior to decontamination.

2.3. Sediment core and soil sampling and processing

The sediment core was sampled using a gravity corer on 8 June 2021 in the downstream part of Mano Dam reservoir (37.72167°N, 140.83056°E) (Fig. 1) 142 *m* below water level by the National Institute of Environmental Studies (Japan). The Mano Dam downstream core (IGSN: 10.58052/IETGC00WU) was 38 *cm* in length with a diameter of 11 *cm* and was sectioned into 38 layers with depth increments of 1 *cm*. Sediment core samples were dried at 40°*C* for 96 h. Soil samples ($n = 68$) were collected in areas representative of the main potential sediment sources according to multiple previous fieldwork campaigns, literature review and stakeholder consultations (Evrard et al., 2015). They were collected as part of Laceby et al. (2016b) study and included 24 undecontaminated cropland, 10 remediated cropland, 24 forest and 10 subsoil (i.e. channel bank or landslide) samples. Soils were sampled with a plastic trowel and consisted of a composite of 10 sub-samples of topsoil (1-2 *cm*). All soil samples were dried at 40 °C for about 48 h and then successively sieved to 2000 μm to remove coarse material, and then to 63 μm to isolate the fraction bearing most of the ^{137}Cs (i.e. silt and clay) and to minimise the effect of grain size sorting along the transport pathway (Walling et al., 2000).

2.4. Laboratory analysis

A set of properties was measured on soil and sediment samples: radiocesium activity by gamma spectrometry (^{134}Cs and ^{137}Cs), organic matter composition determined by the combustion method coupled with an isotope ratio mass spectrometer (i.e. total organic carbon (TOC), total nitrogen (TN), δ^{13}C stable isotope ratio), elemental geochemistry analysed by X-ray fluorescence (ED-XRF) for 17 elements (i.e. Al, Ca, Co, Cr, Cu, Fe, K, Mg, Mn, Ni, Pb, Rb, Si, Sr, Ti, Zn and Zr), visible colourimetry indices by diffuse reflectance (i.e. CIE Lab, CIE LCh), goethite peaks intensity at 445 and 525 *nm* (Debret et al., 2011), the 700 *nm* and 400 *nm* diffuse reflectance ratio (Q7/4; Debret et al. (2011)) and iron oxide-associated parameters derived from the remission function (A1, A2, A3 and Gt; Tiecher et al. (2015)). In addition, bulk density and particle size (grain size frequency, D10, D50, D90) by laser diffraction were measured in all sediment core samples. All analytical methods and calculations are described in the Supplementary Materials A.

2.5. Sediment source fingerprinting

The sediment source fingerprinting technique was conducted considering three potential sources: cropland, forest and subsoil. Subsoil refers to underlying materials exposed along riverbanks or by deep rill or gully erosion, especially under forests (Vandromme et al., 2023). As the main underlying rock is plutonic (48 %, Fig. 1.b), most subsoil and fresh soil originate from the same material (i.e. granite saprolite). In addition, cropland underwent significant changes of properties during decontamination. However, when comparing the source signatures of subsoil and remediated cropland, virtually all properties showed the absence of significant differences (i.e. 25 out of 26 with a p value > 0.01; Supplementary Materials Table B2). Consequently, both sources were merged as subsoil. Care was taken to adjust the interpretation of the source contributions at the light of the progress of decontamination during the different stages of remediation.

2.5.1. Tracer selection

The selection of tracers was performed according to the conventional three-step method (Mukundan et al., 2010; Sellier et al., 2020; Chalaux-Clergue et al., 2024a). The first two steps correspond to the identification of (1) conservative and (2) discriminant properties, subsequently referred to as tracers. Conservative properties were identified with a range test based on the hinge criterion - also referred to as interquartile range (IQR) – (Batista et al., 2022)). To consider a property as conservative, all sediment samples property values should lie within the range defined by source criteria values. The range tests were run using the `range.tests` function from the `fingR` package (Chalaux-Clergue and Bizeul, 2023, ver. 1.1.1). Discriminant properties were identified with the Kolmogorov-Smirnov two-samples test using the `fingR::discriminant.test` function. As Kolmogorov-Smirnov is a sensitive test, two sources were considered statistically different when the p value was below $\alpha = 0.01$. At least two sources must be statistically different to consider the property as discriminant. Finally, (3) a discriminant function analysis (DFA) forward stepwise selection based on Wilk's Lambda criterion was carried out on previously selected tracers (i.e. conservative and discriminant properties) using the function `fingR::stepwise.selection`.

2.5.2. Virtual mixtures

Virtual mixtures were generated to assess modeling accuracy (Palazón et al., 2015; Batista et al., 2022; Chalaux-Clergue et al., 2024a). A total of 138 virtual mixtures were generated using `fingR::VM.builder` (contribution step = 0.05). Within the `fingR::VM.builder` function, the virtual mixture contributions were first designed on a scale from 0 to

100 %, with 5 % increments corresponding to one source group contribution. Then, the two other source groups contributions were determined as fractions of the remaining contribution (i.e. 3/4 for source 2 and 1/4 for source 3). Afterwards, permutations of this contribution scale were determined, which generated a total of 138 unique combinations. Virtual mixture properties were determined as simple proportional mixtures of source property signatures (i.e. mean value). For each property, virtual mixture contributions were multiplied with the source signature and then summed, which provided the virtual mixture property value.

2.5.3. Un-mixing modeling

A multiple-modeling approach was followed to predict source contributions. Multiple-modeling consists of predicting the same property with independent models and then averaging their results. This approach is common in other similar fields of research (Duan et al., 2019; Bruni et al., 2022) and has shown an increase of the prediction quality (Guo et al., 2007). Source contributions were predicted using two common fingerprinting models: MixSIAR and the Bayesian Mean Model (BMM). The MixSIAR model is a Bayesian mixing model, and it was run with the `MixSIAR` package (Stock et al., 2020, ver. 3.1.12) with JAGS (Stock et al., 2022, ver. 4.3.1). The MixSIAR model was set with the "long" Markov Chain Monte Carlo chain length option (i.e. chain length = 300,000, burn-in = 200,000, thin = 100 and chain = 3) with a process error structure. The BMM (Batista et al., 2019) is a bootstrapping approach. It minimises the sum of square residuals of the mixing equation for each iteration of a Monte Carlo simulation ($n = 7500$). The model was constrained to ensure that source contributions were non-negative (lower bound = 0.001) and that their sum equaled 1. Predicted contributions were then re-scaled to 100 % to be expressed as a percentage. Each model convergence was determined by the Gelmand-Rubin diagnosis using the `stable.GR` function from `stableGR` package (Knudson and Vats, 2022, ver. 1.2). None of the approaches had a value greater than 1.06.

2.5.4. Accuracy assessment

Model prediction accuracy was assessed using the contributions predicted for virtual mixtures. The prediction accuracy of each model was evaluated based on different criteria (Chalaux-Clergue et al., 2024a): uncertainty (prediction interval width (W50)), residual error/bias (Mean error (ME)), performance (Squared Pearson correlation coefficient (r^2)), root-mean-square error (RMSE), Nash-Sutcliffe modeling efficiency coefficient (NSE) and continuous ranked probability score (CRPS)). Statistics were calculated using `fingR` functions: `eval.groups` (ME, r^2, RMSE, NSE), `interval.width` (W50) and `CRPS`.

As shown in Chalaux-Clergue et al. (2024a), the comparison of the range of predicted contributions obtained for virtual mixtures and those contributions obtained for actual sediment samples appears to be relevant to assess the transferability of model accuracy metrics calculated with virtual mixtures to actual sediment samples. Indeed, virtual mixtures were generated as simple proportional mixtures of the mean properties of each source tracer. This implies that these tracers showed a strictly conservative behaviour. Therefore, as virtual mixtures were generated to represent a wide range of potential combinations of source contributions, varying from 0 to 100 % with 5-% increments, the range of their predicted contributions was expected to define the minimum and maximum of the possible predicted contributions. The occurrence of predicted contributions of actual sediment samples outside of this range implies the non-respect of some assumptions, such as the potential use of non-fully-conservative tracers. To assess the transferability of the statistics calculated on virtual mixtures to actual sediment samples, the Encompassed Sample Predictions (ESP) was calculated. This value was calculated as the percentage of actual samples for which the predicted contributions remained within the lowest and the highest predicted contributions obtained for the virtual mixtures. When expressed as a percentage, ESP ranges from 0 to 100 %, the latter providing an optimal value. Values close to 100 % indicate a higher transferability of modeling evaluation statistics calculated on virtual mixture to actual sediment samples. ESP values were calculated using `fingR::ESP` function.

All processing, analyses and modeling were performed using the R programming environment (R Core Team, 2022, ver. 4.2.2) within RStudio (RStudio Team, 2023).

2.6. Identifying and dating sedimentation associated to extreme precipitation events

In the Fukushima region, extreme events (i.e. typhoon, tropical storm) that generate daily precipitation exceeding 60 to 100 *mm* (Evrard et al., 2014), have been shown to generate significant ^{137}Cs transfers (Chartin et al., 2013; Laceby et al., 2016a). Therefore, extreme precipitation events have been used as elementary time unit as they are responsible of the majority of sediment transfers, and they took place over short and precise periods of time. According to the study of Huon et al. (2018) in which four sediment were sampled at up-, mid- and downstream locations of the Mano Dam reservoir in November 2014, extreme precipitation events were characterised by the initial deposition of coarser organic-rich material followed by the gradual deposition of finer mineral particles at the downstream location of the Mano reservoir. According to the analysed properties (i.e. organic matter content, element geochemistry, visible colourimetry and grain size), the initiation of sediment deposition following an extreme event should be indicated by higher D10, D50, D90, TOC values, and lower SSA, L*, b*, Al, Si, Ti values, followed by a gradual shift towards the deposition of finer mineral particles. Based on the tipping point of properties between successive events, events can be identified.

The context of the Mano Dam reservoir catchment makes dating of sedimentation events a challenging task. Over the past two decades, the catchment has experienced extreme precipitation events with variable total rainfall depths (from 110 to 396 *mm* (Evrard et al., 2019a)) and different occurrence times during the year (from August to October) as shown in other studies (Laceby et al., 2016a; Evrard et al., 2019a; Vandromme et al., 2023). These differences likely significantly impact sediment transfers across the catchment and associated sediment records in the lake (Evrard et al., 2016). Furthermore, rapid changes in anthropogenic activities associated with decontamination have modified soil sensitivity to erosion and its composition (Feng et al., 2022; Evrard et al., 2019b). Following the evacuation of the area in July 2011 and its reopening to the population in March 2017 (MoE, 2018), the region remained devoid of human activity for 6 years and 9 months until decontamination was carried out. Most of this remediation took place between mid-October and December 2016, with 80 % of the remediated area being decontaminated during this period (Vandromme et al., 2023). Despite the reopening, the return of population and agricultural activities remain limited (Asanuma-Brice et al., 2023), allowing for natural vegetation to develop again after decontamination.

Accordingly, the identified events were dated by combining their ^{137}Cs activity distribution along the sediment core, and their comparison with that found in previously studied sediment cores (Huon et al., 2018), daily precipitation records and information on the progress of decontamination. The identification and dating of successive events was done within the Results section of the manuscript (Sec. 3.1.6 and 3.2.5) to further calculate and understand calculation of the properties of the events (^{137} activity and deposition flux per event, sediment transfer, and source contribution per event) without discussing it. However, the identification and dating were discussed within the Discussion section (Sec. 4.1).

2.7. Extreme events averaged properties

After identification of successive sedimentation events in the sediment core, the average ^{137}Cs activity and source contributions of the entire extreme event were calculated. To do this, each sediment layer and the total event density were taken into account using the following formula:

$$X_{\text{event}} = \sum_{i=1}^{n} \frac{\rho_i}{\rho_{\text{event}}} X_i \quad \text{with} \quad \rho_{\text{event}} = \frac{\sum_{i=1}^{n} \rho_i}{t_{\text{event}}} \tag{1}$$

With ρ the density ($g\,cm^{-3}$), t the layer thickness (cm), and X the property value of, respectively, the sediment layer i or the *event*, with n the number of sampling layers within the extreme event.

In addition, the Mass Accumulation Rate (MAR) for the core was calculated for each identified extreme event (expressed in $g\,cm^{-2}\,event^{-1}$). The MAR was calculated as the product of each event sedimentation accumulation rate (SAR, in $cm\,event^{-1}$), corresponding to the quantity of sediment transported per extreme event or in other terms the event thickness in the core in cm, and the event bulk density (ρ_{event}, in $g\,cm^{-3}$).

$$\text{MAR}_{\text{event}} = SAR_{\text{event}} \cdot \rho_{\text{event}} \tag{2}$$

Using the predicted contributions of the potential sources, the quantitative contribution of each source was calculated as the product of relative contributions and MAR values. Finally, the ^{137}Cs deposition flux per extreme event (in $Bq\,m^{-2}\,event^{-1}$) was calculated, as the product of the extreme event MAR and ^{137}Cs activity.

$$\text{Flux}_X = \text{MAR}_{\text{event}} \cdot X_{\text{event}} \tag{3}$$

3. Results

3.1. Identifying sedimentation events

3.1.1. Sediment core description

The sediment core displayed a pattern of fine sediment deposition (in average D50 = 23.4 ± 12.8 μm (SD)), with alternating darker and lighter brown layers. About six darker layers were identified from 5.4 to 28.7 cm depths, averaging 1.9 ± 0.9 cm (SD) of thickness (Fig. 2.a). Notably, two layers exhibited coarse plant debris from leaves or litter, just below a darker brown layer (i.e. at 10.1 and 13.8 cm). The unit between 19.6 – 22.1 cm, which contains two dark layers, 19.6 – 20.3 cm and 21.1 – 22.1 cm, appeared to be slightly disturbed as the layer was locally diffuse and lightly irregular. This was likely the result of the following extreme precipitation event. The most recent sediment, from the top to 6/7 cm, was lighter brown and more yellow than the nearby underlying sediments and closer to that of older sediments found below 28 cm. This was confirmed by their higher b* and L* values, about 16 % and 9 %, than the mean values for sediment between 7 to 28 cm (i.e. 12.4 ± 0.8 versus 10.7 ± 0.9, and 49.7 ± 0.9 versus 45.5 ± 2.6, respectively) (Fig. 2.a and b).

3.1.2. Radiocesium activities

The ^{134}Cs/^{137}Cs ratio from 22 cm to the top of the sediment core remained within the range of 1.06 ± 0.04 (SD) attributed to material exposed to Fukushima fallout (Kobayashi et al., 2013) (Fig. 2.d). Consequently, sediment layers above 22 cm were inferred to have deposited after the FDNPP accident.

The depth distribution profile of ^{137}Cs was characterised by a distinct peak of about 50 $kBq\,kg^{-1}$ at 17 – 18 cm depth (Fig. 2.e). Below this peak, the ^{137}Cs activity exponentially decreased until reaching a stable level of about ten $Bq\,kg^{-1}$ (i.e. from 7 to 19 $Bq\,kg^{-1}$) for layers deeper than 32 cm, consistent with expected pre-accidental levels (Fukuyama et al., 2010). Conversely, above this peak, from 14 to 11 cm, activities rapidly decreased down to a plateau of about 13 ± 0.5 $kBq\,kg^{-1}$ (SD). Following this, a gradual decrease of activity was observed from 8 to 5 cm, with the ^{137}Cs activity decreasing from 9.7 to 2.3 $kBq\,kg^{-1}$, then reaching a lower plateau of about 2.2 ± 0.2 $kBq\,kg^{-1}$ (SD) from 5 cm depth to the top of the sediment core.

3.1.3. Elemental geochemistry

Among the geochemical elements analysed, Al, Si, and Ti showed similar variations along the sediment core, with Ti showing lower variations (Fig. 2.f, g, and h). Along the sediment core, four zones (i.e. 9–10, 12–14, 19–21, 25 – 27 cm) were characterised by a decrease of concentrations in these elements, with reductions of 11 %, 13 %, and 5 %,

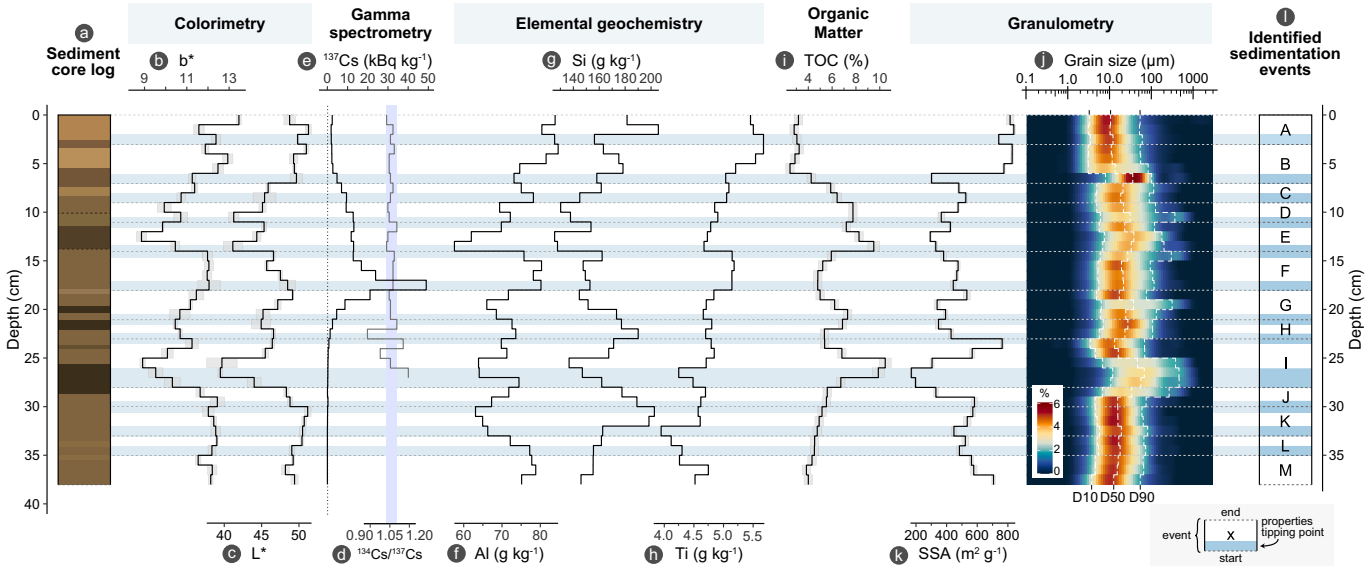

Fig. 2. Mano Dam reservoir (a) sediment core log and analysed properties, from left to right: colour indices: (b) L* and (c) b*, (d) ^{134}Cs/^{137}Cs ratio decay-corrected to 11 March 2011 along with the 1.06 ± 0.04 (standard deviation) range attributed to material exposed to Fukushima fallout (blue area) (Kobayashi et al., 2013), (e) ^{137}Cs activity, elemental geochemistry of: (f) Al, (g) Si, (h) Ti, (i) total organic carbon (TOC) content, and granulometry: (j) frequency of grain size from 0.1 to 2500 μm along with the D10, D50 and D90 (white dashed lines) and (k) specific surface area (SSA), and (l) identified extreme precipitation events. Measurement uncertainties are displayed as a grey ribbon.

respectively, compared to the surrounding layers. Furthermore, the most recently deposited sediments, from 5 *cm* depth to the top of the core, showed marked increases in Al and Ti concentrations, by 15 % and 17 %, respectively, compared to previously deposited sediments (Fig. 2.g and h).

3.1.4. Organic matter

The TOC content varied along the sediment, and was characterised by four distinct peaks (i.e. 9 – 11 *cm*, 12 – 15 *cm*, 20 – 22 *cm*, and 25 – 27 *cm*) of higher TOC contents, with an increase from about 39 % to 100 % (ranging from 7.1 to 10.2 ± 0.4% (SD)) compared to the surrounding sediments (i.e. 5.1 ± 0.8% (SD)) (Fig. 2.i). In addition, the sediment from 6 *cm* to the top of the sediment core exhibited significantly lower TOC contents averaging 2.9 ± 0.3%, which was 59 % lower than for previously deposited sediment.

3.1.5. Grain size and specific surface area

Along the sediment core, distinct peaks of coarser grain size and lower SSA were identified (i.e. 10 – 11 *cm*, 14 – 15 *cm*, 19 – 20 *cm* and 25 – 29 *cm*) (Fig. 2.j and k). These peaks were characterised by a sharp

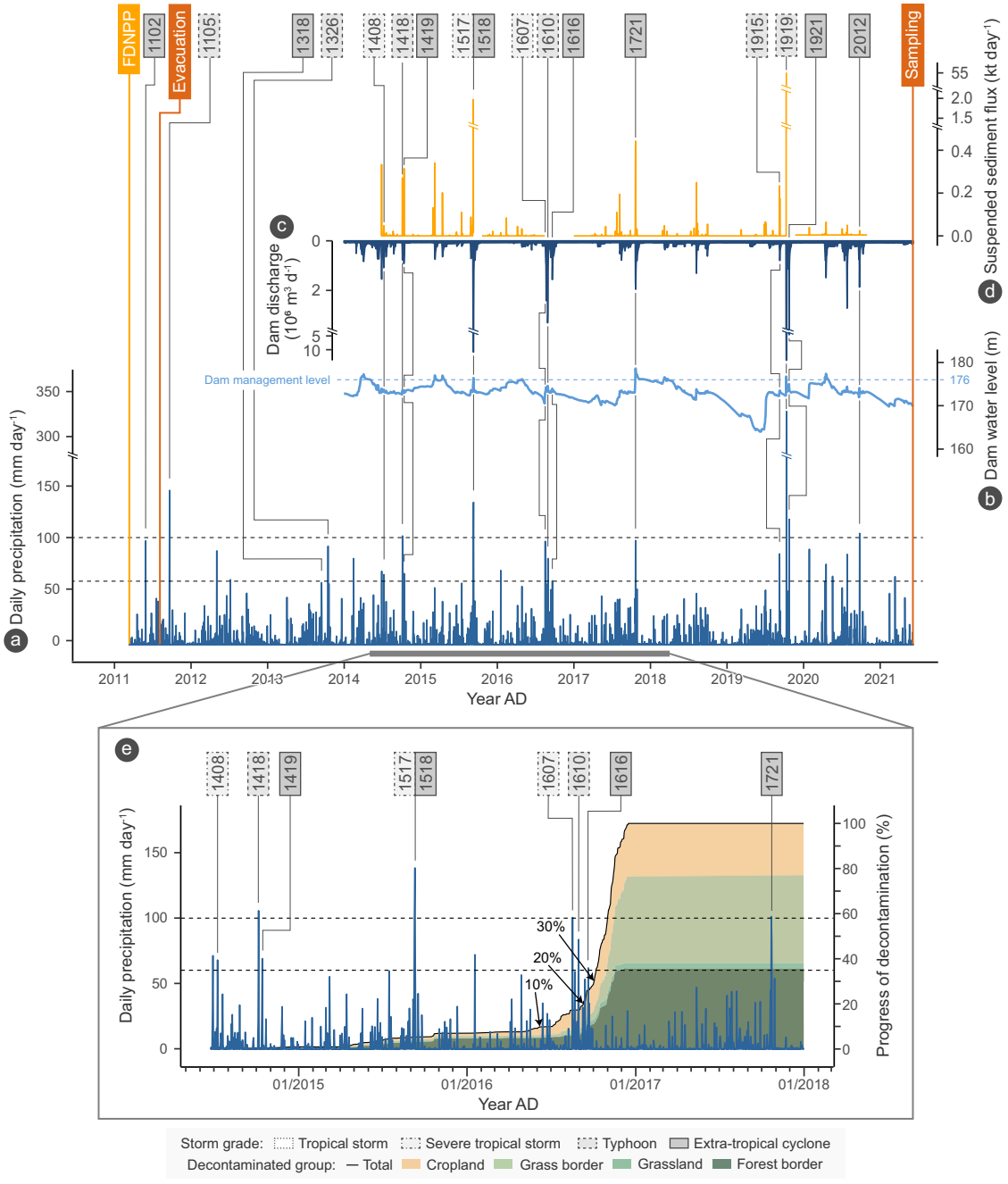

Fig. 3. (a) Mean daily precipitation at the four precipitation monitoring AMeDAS stations surrounding the Mano Dam reservoir catchment between March 2011 and June 2021, reservoir dam (b) water level and (c) water discharge between January 2014 and June 2021, (d) suspended sediment flux at the hydrological station upstream the reservoir, and (e) the progress of decontamination as of cumulative proportion of the total decontaminated area under contrasted land uses (cropland, grass border, grassland, forest border). Extreme precipitation events ranked as extra-tropical cyclone (solid), typhoon (dash), severe tropical storm (dot-dash) and tropical storm (dot) that generated more than 60 or 100 *mm* of daily precipitation (horizontal dotted lines, Evrard et al. (2014)) are identified by their international number ID. The progress of the total decontaminated surface area with the successive levels of 10 %, 20 % and 30 % are indicated. The grey bar in sub-figure (a) represents the time frame displayed in sub-figure (b).

increase of D50 and D90 values, in average, by about 130 % and 280 %, respectively, a moderate increase of D10 (by about 47 %), and a decreased SSA by about 36 %, compared to surrounding sediment layers ($D10 = 5 \pm 1\ \mu m$, $D50 = 20 \pm 6\ \mu m$, $D90 = 96 \pm 37\ \mu m$, $SSA = 516 \pm 101\ m^2\ g^{-1}$). These peaks, for which mainly D50, D90 and SSA varied, were likely to reflect a greater amount of coarse particles.

In addition, sediment from 7 to 15 *cm* showed less uniform grain size distribution compared to underlying sediments (< 30 *cm*), despite a less marked variation of SSA. This suggests a greater frequency of recorded events than deeper in the sediment core (i.e. more events over a shorter depth) as well as the supply of more similar material (Fig. 2.j).

Conversely, the most recently deposited sediments, from 5/6 *cm* to the top of the sediment core, showed a high homogeneity with fine sediment, comparable to that of sediment below 29 *cm*. However, their grain sizes were found to be the lowest along the sediment core ($D10 = 3 \pm 0\ \mu m$, $D50 = 11 \pm 1\ \mu m$, and $D90 = 59 \pm 11\ \mu m$), and they showed the highest SSA ($816 \pm 24\ m^2\ g^{-1}$).

3.1.6. Identifying sedimentation events along the sediment core

According to the comparison of the properties, including elemental geochemistry, organic matter, visible colourimetry and grain size, and criteria defined in Sec. 2.6 a total of 13 sedimentary events were identified along the sediment core, systematically labelled alphabetically from the top to the bottom (Fig. 2.l).

3.2. Dating of events

3.2.1. Identification of extreme precipitation events

From the FDNPP accident in March 2011 to the sediment core sampling in June 2021, 27 and 6 extreme precipitation events that generated more than 60 or 100 $mm\ d^{-1}$ of daily precipitation, respectively, were identified (Fig. 3.a). Of these, 17 were major tropical storms and typhoons (Fig. 3.a; Supplementary Materials Table B1). While some years were devoid of extreme precipitation events (i.e. 2012 and 2018), most years recorded one such event (i.e. 2017 and 2020), other years recorded two (i.e. 2013 and 2015) or even three events (i.e. 2014, 2016 and 2019).

Among the 27 extreme precipitation events, 16 events led to exceptionally high cumulative precipitation exceeding 100 *mm*. Among those 16 events only six events yielded cumulative precipitation exceeding 150 *mm*: typhoon Roke in September 2011 (ID: 1105 - 259 *mm*), extra-tropical cyclone Etau in September 2015 (ID: 1518 - 396 *mm*), tropical storm Chanthu (ID: 1607 - 197 *mm*) and severe tropical storm Lionrock (ID: 1610 - 157 *mm*) in August 2016, extra-tropical cyclone Lan in October 2017 (ID: 1721 - 264 *mm*) and typhoon Hagibis in October 2019 (ID: 1919 - 372 *mm*). Moreover, some events occurred successively within a 10-days period, such as typhoon Phanfone (ID: 1418 - 130 *mm*) and extra-tropical storm Vongfong (ID: 1419 - 94 *mm*) in October 2014, Chanthu and Lionrock in August 2016, and Hagibis and extra-tropical cyclone Bualoi (ID: 1921 - 129 *mm*) in October 2019.

3.2.2. Extreme precipitation events and reservoir management

Extreme precipitation events that generated more than 60 *mm* of daily precipitation consistently led to daily water discharges exceeding the usual discharges (i.e. $87 \times 10^3\ m^3\ d^{-1}$; Fig. 3.a, b and c). The extreme precipitation events of 2014, 2017 and 2020, which had equivalent precipitation levels, led to similar water discharges by dam operators (about 20-30 $m^3\ s^{-1}$; Fig. 3.a and c; Supplementary Materials Table B4). However, the 2016 event, characterised by a series of moderate extreme precipitation events (daily precipitation between 60 and 100 *mm*; Fig. 3.a), resulted in higher water discharges and a prolonged discharge period (35.8 versus about 19.5 $m^3\ s^{-1}$ on average; Fig. 3.c; Supplementary Materials Table B4) despite relatively low dam water levels (Fig. 3.b). The exceptionally high cumulative precipitation events of 2015 and 2019 led to maximum daily water discharges that were two to ten times higher than those associated with the 2014, 2016, 2017 and 2020 events (203.3 and 364.8 $m^3\ s^{-1}$, respectively; Supplementary Materials Table B4).

Water level management procedures different significantly depending on the amount of precipitation during an extreme event (Supplementary Material Fig. B2 and Table B4). In 2015 and 2019, during higher-magnitude precipitation events, water level of the dam systematically exceeded the water level management threshold (i.e. 176 *m*). Dam operators responded rapidly to this increased water inflow (max. 349.3 and 695.0 $m^3\ s^{-1}$ versus from 40 to 200 $m^3\ s^{-1}$ for lower-magnitude events; Supplementary Materials Table B4), leading to large variations in water levels over a short period, about 4.9 and 7.3 *m* (max. water level 177.6 and 179.5 *m*), respectively. During the 2015 events, it took about 12 *h* to return below the water level management threshold and 15 *h* for the 2019 event. Conversely, lower-magnitude events, such as those that occurred in 2014, 2017, and 2020, which showed lower inflows, only the 2017 event exceeded the water level management threshold (max. 178.9 *m*). This pattern allowed for a smoother dam management and more gradual water level changes, about 1.4 to 4.1 *m* managed from two to more than four days. However, despite the fact that the 2017 event was associated with a large water level change of 5.9 *m* (max. water level 178.9 *m*), dam management was not associated with large water discharge, and it took 16 days to return to the management level.

3.2.3. Suspended sediment flux to the reservoir

Over the recorded period, significant suspended sediment fluxes at the reservoir inlet were highly associated with extreme precipitation events and occurred over a short period of time (Fig. 3.d). Some isolated precipitation events, with daily precipitation below 60 *mm*, resulted in some sediment transfer. These events were always associated with higher than usual water discharges (Fig. 3.c and d). The lower-magnitude events of 2014, 2017 and 2020, which had similar precipitation levels, led to different maximum suspended sediment fluxes: about 12 to 20.4 $kg\ s^{-1}$ and 20.5 $kg\ s^{-1}$ in 2014 and 2017, respectively, and 0.5 $kg\ s^{-1}$ in 2020 (Fig. 3.d; Supplementary Materials Table B4). The higher-magnitude events of 2015 and 2019, resulted in maximum suspended sediment fluxes of 169.7 and 7495.1 $kg\ s^{-1}$, until the monitoring stations were damaged, which was about 10 and 430 times higher than those observed on average during lower-magnitude events.

3.2.4. Decontamination progress and extreme rainfall events

From June 2014 to December 2016 (i.e. 31 months), a total of 8.2 km^2 underwent decontamination, representing 12 % of the total catchment area of the Mano Dam reservoir (Fig. 3.e). Within the decontaminated area, the majority (66 %) of the operations did not involve the addition of fresh soil, as it concentrated in the remediation of grass borders (i.e. grass strips adjacent to cultivated plots, nearby roads, and houses) (3.2 km^2, 39 %), forest borders (2.9 km^2, 35 %) and grassland (0.2 km^2, 2 %). Remediated cropland accounted for 1.8 km^2, representing only 22 % of the total decontaminated area and 3 % of the total catchment area. Most of the decontamination (80 %) occurred in the last four months of 2016, from 10 September to 31 December. In contrast, only 10 % of the total area underwent decontamination during the 25 months that occurred between the initiation of decontamination in June 2014 and 7 July 2016.

Until mid-2016, the progress of decontamination remained limited, and affected a marginal area which was unlikely to be reflected in sediment records associated to extreme precipitation events that occurred since 2014 (Fig. 3.e). However, in the six weeks preceding the occurrence of Chanthu and Lionrock events in August 2016, significant progress was made in decontamination, mainly under cropland. Within this period, an additional 0.44 km^2 of cropland was decontaminated, representing 24 % of the total area of decontaminated cropland and 5 %

of the catchment area. Conversely, over the 26 months since the initiation of decontamination, only 0.29 km^2 (16 %) had been decontaminated. However, the majority of decontamination (83 %) was carried out after the two extreme events that occurred in August 2016 (Chanthu and Lionrock). Following the completion of decontamination in December 2016, the subsequent extreme precipitation event, Lan, occurred in October 2017.

3.2.5. *Dating of identified sedimentation events*

The sediment core analysis revealed a single peak of ^{137}Cs activity at 17–18 *cm* layer, indicating the occurrence of the FDNPP accident (Fig. 2.d). The exponential decrease of ^{137}Cs activity below the 17–18 *cm* layer suggest downward diffusion over time as observed in other lacustrine sediment cores (Cao et al., 2017; Funaki et al., 2022). This peak aligned with sedimentation event F (from 14 to 18 *cm*, Fig. 2.k), suggesting that all the sedimentation events below it occurred prior to March 2011. In relation to the objectives of the study, among all the sedimentation events identified in Section 3.1.6, events G through M were not assigned to specific extreme precipitation events.

In September 2011, typhoon Roke generated exceptionally high cumulative precipitation (Fig. 3.a and Supplementary Materials Table B3). This event, resulted in significant sediment transfers in response to a high hydro-sedimentary connectivity (Chartin et al., 2017) and high erosivity (Laceby et al., 2016a). Consequently, the event F was associated with the occurrence of Roke in September 2011 (Fig. 4).

In addition, in November 2014, Huon et al. (2018) collected two sediment cores (referred to as DD1 and DD2) at the same location as the core analysed in the current study. When comparing the distribution of ^{137}Cs activity and TOC content between these sediment cores revealed high similarities between the DD1 0 – 30 *cm* and DD2 0 – 15 *cm* sections and the 11-24 *cm* section of our sediment core (Supplementary Materials Fig. B1). This suggests that the sediment deposition below 10 *cm* occurred before November 2014. Thereafter, between event F and 10 *cm* depth, only one event was identified, event E (Fig. 4). While no extreme event occurred in 2012, two events took place in 2013 and two more in 2014. Although 2013 and 2014 were affected by events of similar intensity, the events in 2014 occurred within a 10 days period and later in the year (October) than in 2013 (September and October). Events occurring close together were more likely to generate erosion due to soil saturation. In addition, as the events in 2014 occurred later in the year, the vegetation cover was less developed and therefore less prone to protect the soil from erosion. Accordingly, event E was associated with the occurrence of typhoons Phanfone & Vongfong in October 2014 (Fig. 4).

In the Mano Dam reservoir catchment, after 2014, the next significant change in terms of land use was the implementation of decontamination. As most of the decontamination took place at the end of 2016 and after the extreme precipitation events of the year, the effects of decontamination could only be visible from the subsequent year events (i.e. from 2017) (Fig. 3). Notably, within the sediment core, an abrupt change of properties was observed for sediment from 0 to 7 *cm* depth, contrasting with previously deposited sediment layers (Fig. 2). Moreover, their properties tended towards those characteristics of subsoil or fresh soil (Fig. 2; Supplementary Materials Table B3), which suggests that decontamination had occurred before their deposition (Evrard et al., 2019a; Feng et al., 2022). Within this interval, two sedimentation events were identified: events A and B (Fig. 2). Subsequently, between 2017 and the sediment core sampling in June 2021, only two major precipitation events occurred: Lan in 2017 and Hagibis & Bualoi in 2019 (Fig. 3). In 2017, although Lan was a moderate event in terms of cumulative precipitation, it generated a higher suspended sediment flux than previous equivalent events (i.e., versus 2014 events; Fig. 3.a and c).

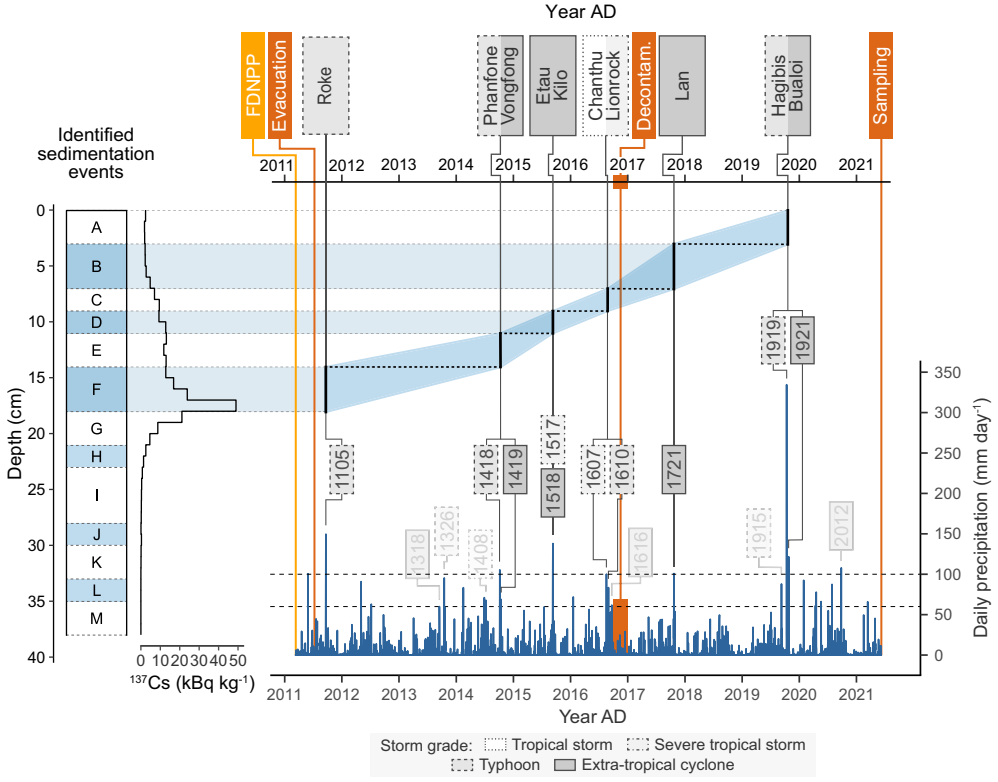

Fig. 4. (a) Identification of extreme precipitation events-associated deposits and (b) dating of these identified deposits by comparing ^{137}Cs distribution along the sediment core, progress of decontamination, and the extreme precipitation events that occurred since the Fukushima Daiichi Nuclear Power Plant (FDNPP) accident in March 2011. Decontam. stands for decontamination. Extreme precipitation events ranked as extra-tropical cyclone (solid), typhoon (dash), severe tropical storm (dot-dash) and tropical storm (dot) that generated more than 60 *mm* of daily precipitation (horizontal dotted line, Evrard et al. (2014)) are identified by their international number ID and named when associated with a deposit.

In addition, the dam operators operated a moderate water discharges and kept the water level at the management level for the next six months (i.e. about 175-176 *m* until April 2018; Fig. 3.b and c), which likely allowed the deposition of a large proportion of the eroded sediment. In contrast, in 2019, Hagibis & Bualoi generated large cumulative precipitation and large suspended sediment fluxes at the reservoir inlet (Fig. 3.a and d). The dam operators therefore operated large water releases and managed the water level to rapidly return to about 173 *m* (Fig. 3.b and c). This water level management likely accelerated water flow within the reservoir and thus limited sediment deposition. Hagibis & Bualoi was likely under-represented in the sediment record. In summary, both events, Lan and Hagibis & Bualoi, were likely recorded in the sediment. Despite the moderate intensity of Lan, dam management likely allowed better sedimentation during this event than during Hagibis & Bualoi. Therefore, Lan and Hagibis & Bualoi events were associated with sedimentation events B and A, respectively (Fig. 4).

Lastly, two sedimentation events were identified between 7 and 14 *cm*: event C and D. Corresponding to the dating of events discussed earlier, these events occurred between early 2015 and mid-2016. In October 2015, the simultaneous occurrence of Etau and Kilo generated high precipitation and erosivity (Laceby et al. (2016a); Fig. 3.a), which resulted in large suspended sediment fluxes at the reservoir inlet (Fig. 3.d). The dam operators therefore operated large water releases and managed the water level to rapidly return to about 173 *m* (Fig. 3.b and c), which likely limited sediment deposition. In contrast, August 2016, Chanthu & Lionrock were two moderate events that occurred within a 10 days period. The dam operators operated moderate water discharge and remained well below management level (Fig. 3.c), which likely affected to a limited extent sediment deposition. In addition, Chanthu & Lionrock occurred just before the acceleration of decontamination. Consequently, the sedimentation events C and D were associated to Etau-Kilo in October 2015 and Chanthu & Lionrock in August 2016, respectively (Fig. 4).

3.3. Source sediment fingerprinting

3.3.1. Origin of organic matter

Undecontaminated cropland, remediated cropland, and subsoil had similar $\delta^{13}C$ mean values, respectively, with -25.0 ± 1.1 ‰ (SD) (range: -27.7 ‰ to -22.9 ± 0.1‰), -24.4 ± 1.5‰ (-26.2 ‰ to -22.0 ± 0.1‰) and -25.4 ± 1.0‰ (-27.0 ‰ to -23.6 ± 0.1‰) (Fig. 5 and Supplementary Materials Table B1 and B2). However, the $\delta^{13}C$ values of the forest were significantly lower than those of undecontaminated and remediated cropland, -26.3 ± 1.1‰ (-27.8 ‰ to -23.5 ± 0.1‰) (Supplementary Materials Table B1 and B2).

Conversely, with the exception of subsoil and remediated cropland, all sources differed significantly in TOC/TN values (Supplementary Materials Table B1 and B2). Forest had the highest TOC/TN values with a mean of 15.4 ± 2.3 (SD) (range: 9.8 to 19.7 ± 2.1), followed by undecontaminated cropland ($11.9 \pm 1.4 - 9.6$ to 16.3 ± 2.1), subsoil ($11.6 \pm 1.6 - 8.2$ to 13.5 ± 2.1) and remediated cropland ($10.3 \pm 2.0 - 6.3$ to 13.0 ± 2.1) in decreasing order (Fig. 5). Remediated cropland and subsoil and cropland signals were closer to the soil organic matter signature, while that of forest was closer to plant debris signature. The $\delta^{13}C$ and TOC/TN values of the sediment samples were included within the range of values found in potential sources, with the exception of three samples (Fig. 5). The $\delta^{13}C$ values of the sediment samples varied from -28.65 ‰ to -24.68 ± 0.04‰, and their TOC/TN values changed

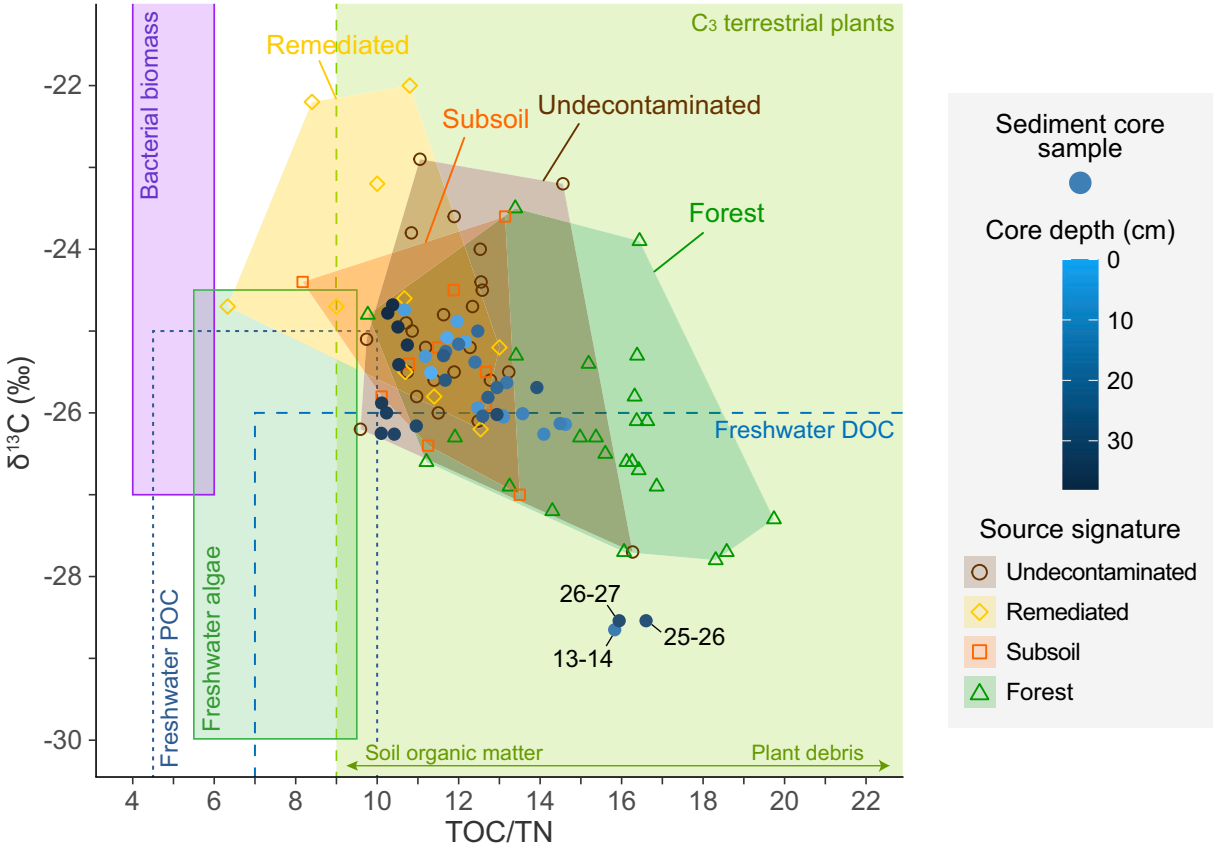

Fig. 5. Signatures of $\delta^{13}C$ and TOC/TN in potential sources and in sediment core samples along with typical ranges for organic inputs to clay-sized dominant terrestrial environments (according to Lamb et al. (2006) and Amorim et al. (2022)). Sediment core samples showing values lying outside of the range found in potential sources are indicated by their depth intervals (*cm*). TOC stands for total organic carbon; POC for particulate organic matter; DOC for dissolved organic matter.

from 10.1 % to 16.6 ± 2.1%. However, three sediment samples lied outside of the space defined by potential sources (i.e. 13–14, 25–26 and 26 − 27 *cm*). These three sediment samples were similar and characterised by very low $\delta^{13}C$ values (respectively −28.65 ‰, −28.54 ‰ and -28.54 ± 0.04‰) and high TOC/TN values (respectively 15.8 %, 16.6 % and 15.9 ± 2.1%). However, all the sediment samples had signatures plotting within the range of typical C_3 terrestrial plants organic inputs (Fig. 5) (Lamb et al., 2006; Amorim et al., 2022).

3.3.2. Tracer selection

Of the 24 properties measured and analysed on potential source soil samples and sediment core layers (Supplementary Materials Table B3), only ten were found to show a conservative behaviour when tested according to the hinge criterion range test (TOC, TN, Al, Si, Ti, L*, b*, C*, Q7/4, G_{525}) (Fig. 6). Among these ten conservative properties, only Ti did not significantly (p value < 0.01) discriminate between potential sources (i.e. cropland, forest, subsoil). This resulted in the selection of eight tracers. These tracers consist of two organic matter parameters (TOC, TN), two geochemical elements (Al, Si) and five colour parameters (L*, b*, C*) and indices (Q7/4, G_{525}). Among the eight potential tracers, a suite of four tracers was selected by the DFA stepwise selection (Al, Si, b*, C*).

Different levels of source discrimination were observed among the eight tracers. Half of the tracers provided strong and equivalent discrimination capacity of the potential sources (TOC, TN, Al, L*, G_{525}). Conversely, the other half did not significantly discriminate between forest and undecontaminated cropland sources (Si, b*, C*). Therefore, sediment source fingerprinting modeling was run using the tracer selection obtained prior to DFA stepwise selection (TOC, TN, Al, Si, Ti, L*, b*, C*, Q7/4, G_{525}).

3.3.3. Sediment source fingerprinting modeling

Modeling accuracy metrics obtained with MixSIAR and BMM were strongly similar among sources (Supplementary Materials Table B5). The largest differences were found in terms of model performance for undecontaminated cropland and forest. In any case, results were better for the multiple model approach than those obtained with each model run independently. On average, the multiple model bias (ME) and linearity (r^2) were intermediate, whereas accuracy (RMSE) and modeling efficiency (NSE) were slightly higher than for the individual model approach.

Regarding the relationship between the theoretical and the predicted contributions for the virtual mixtures, different tendencies were observed (Fig. 7.a, b and c). The subsoil and forest contributions were well predicted, despite that forest tended to be under-predicted above 30 % of theoretical contributions (Fig. 7.b and c). The undecontaminated cropland contributions prediction quality was lower although being rather linear, and were over-predicted below 40 % of theoretical contributions and under-predicted above it (Fig. 7.a).

When evaluating the transferability of the model accuracy metrics derived from virtual mixture predictions to those of actual sediment samples, notable differences were found across sources (Fig. 7.a, b and c). The actual sediment samples predictions for undecontaminated cropland and forest contributions closely aligned with those from virtual mixtures, with ESP of 100 % and 92 %, while subsoil predictions exhibited lower consistency, with ESP of 66 % (Supplementary Materials Table B4). However, when considering theoretical and predicted contributions of virtual mixtures simultaneously for all three sources (Fig. 7.d), the predicted contribution space appeared contracted compared to the initial theoretical space. This contraction was mainly related to the narrower range of predicted contributions for uncontaminated cropland (from 4 % to 69 %), and the lower maximum for forest contributions (73 %). Only three out of 38 sediment samples had predicted contributions within the virtual mixtures space, about 15 samples were close to this space. Sediment samples located the furthest from this space were characterised by low predicted subsoil contributions (< 10 %) and balanced contributions from forest and uncontaminated cropland. Modeling accuracy metrics are therefore likely not fully transferable to model outputs obtained for actual sediment samples.

3.4. Evolution of sediment transfers and sources throughout time

Following the accident, there were notable changes in both the quantitative (MAR) and qualitative (sources) sediment transfer pattern associated to extreme precipitation events (Fig. 8.a). The first typhoon following the accident, Roke in September 2011, likely reflected the pre-accidental sources contributions, characterised by a cropland dominance (about 54 %), followed by forest (about 35 %) and subsoil (about 10 %) (Fig. 8.a; Supplementary Materials Table B6). However, this event resulted in sediment accumulation about twice-fold compared to pre-accidental levels (MAR = 1.87 versus 0.96 ± 0.25 $g\ cm^{-2}\ event^{-1}$). This significant increased sediment deposition was likely a consequence of the intensity of the event and the landscape disturbances after the Great Tohoku Earthquake, including landslides and bank collapses, which have not been immediately dealt with given the subsequent evacuation order (July 2011).

During the abandonment period, the three sedimentation events that occurred (2014, 2015 and 2016) were characterised by MAR values closer to pre-accidental levels although they showed significant changes in source contributions. In 2014 and 2015, there was a significant

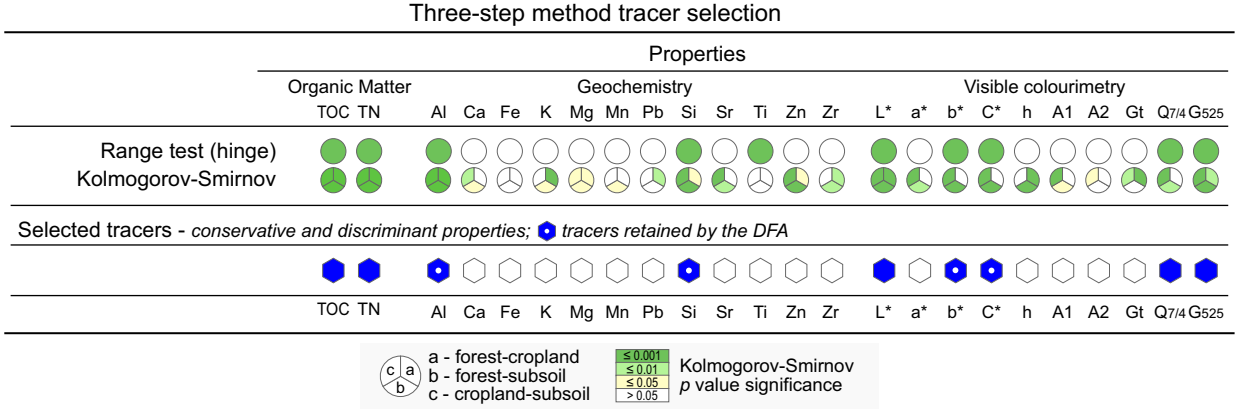

Fig. 6. Tracer selection according to the Three-Step Method using range test hinge criteria. Green filled circles and portions indicate a property that passed the conservativity (i.e. range test) and the discriminant power (i.e. Kolmogorov-Smirnov two-samples test p value < 0.01) tests, respectively. Blue filled diamonds indicate selected tracers (i.e. properties that passed both conservativity and discriminant power tests) and blue diamonds with white dots indicate tracers retained by the discriminant function analysis (DFA) forward stepwise selection based on Wilk's lambda criterion. TOC stands for total organic carbon.

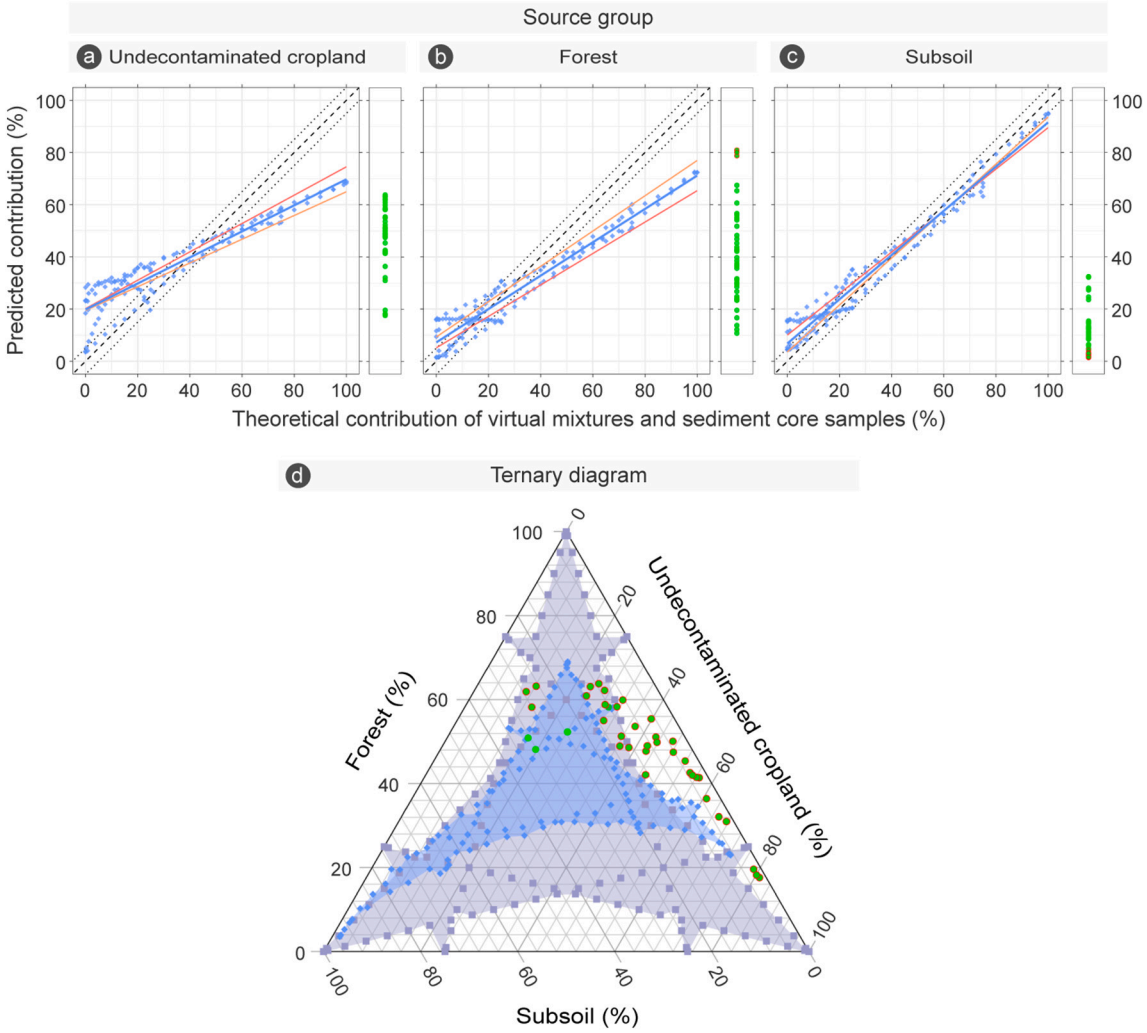

Fig. 7. Relationship between theoretical and predicted contributions of the virtual mixtures (blue diamond) for each source: (a) undecontaminated cropland, (b) forest, (c) subsoil, of the multiple model (blue line) as the average of MixSIAR (red line) and Bayesian Mean Model (orange line) predictions along with actual Mano Dam sediment core samples predicted contributions (green circle). (d) Ternary plot of the theoretical (light blue diamond) and predicted (blue diamond) contributions of the virtual mixtures and predicted contributions of the Mano Dam sediment core samples (green dot). Mano Dam sediment core samples with predicted contributions outside of the range/space defined by the predicted contributions of the virtual mixtures are circled in red.

decrease of quantitative contributions of undecontaminated cropland (24 % and 39 %), while those of forest increased (41 % and 11 %) compared to pre-accidental levels. Conversely, in 2016, the MAR slightly increased compared to 2015 (6 %), along with an increase of the quantitative contribution of undecontaminated cropland (43 %). This trend likely resulted from the occurrence of some decontamination shortly before the occurrence of 2016 precipitation events, which left the soil bare and vulnerable to rainfall and runoff.

After the completion of decontamination, the events of 2017 and 2019 were characterised by a significant increase in sediment transfers, with their MAR values reaching 270 % and 190 % of the pre-accidental levels despite the intensity of the 2017 event that was similar to that of 2016 events (Fig. 3; Supplementary Materials Table B7). This massive increase of sediment transfer was associated with a drastic increase in the quantitative contribution from subsoil (+180 % and + 108 %) and undecontaminated cropland (625 % and 419 %), while contribution of forest remained similar to pre-accidental levels.

3.5. Evolution of ^{137}Cs transfers through time

Throughout each event, the ^{137}Cs activity in the sediment has consistently decreased (Fig. 8.b; Supplementary Materials Table B7). From 2011 to 2016, the activity gradually decreased over time, almost following an exponential decay, with reductions of about 20 %, 15 %, and 27 % per year between 2011–2014, 2014–2015 and 2015–2016, respectively, averaging 21 % per year between 2011 and 2016 events. Following the completion of decontamination, there was a notable drop of 65 % in ^{137}Cs activities between 2016–2017 events, equivalent to a decrease of 56 % per year. Subsequently, there was again a gradual decrease of 28 % between 2017 and 2019, equivalent to a decrease of about 14 % per year. Over the period from the initial extreme precipitation event post-accident in 2011 to the most recent events in 2017 and 2019, ^{137}Cs activities decreased significantly by about 89 % to 92 % (26.1 versus 2.9 and 2.1 $kBq\,kg^{-1}\,event^{-1}$ respectively), which was equivalent to a decrease of about 30 % and 26 % per year, respectively.

Conversely, the evolution of total ^{137}Cs deposition flux per event did not fully reflect the same trends as that of ^{137}Cs activities (Fig. 8.c; Supplementary Materials Table B7). From 2011 to 2016, the decrease trend was similar, with reductions of about 30 %, 45 % and 22 % per year between 2011–2014, 2014–2015 and 2015–2016, respectively, averaging 32 % per year between 2011 and 2016 events. Conversely, following the completion of decontamination, the ^{137}Cs deposition flux in 2017 remained unchanged from that of 2016 (i.e.

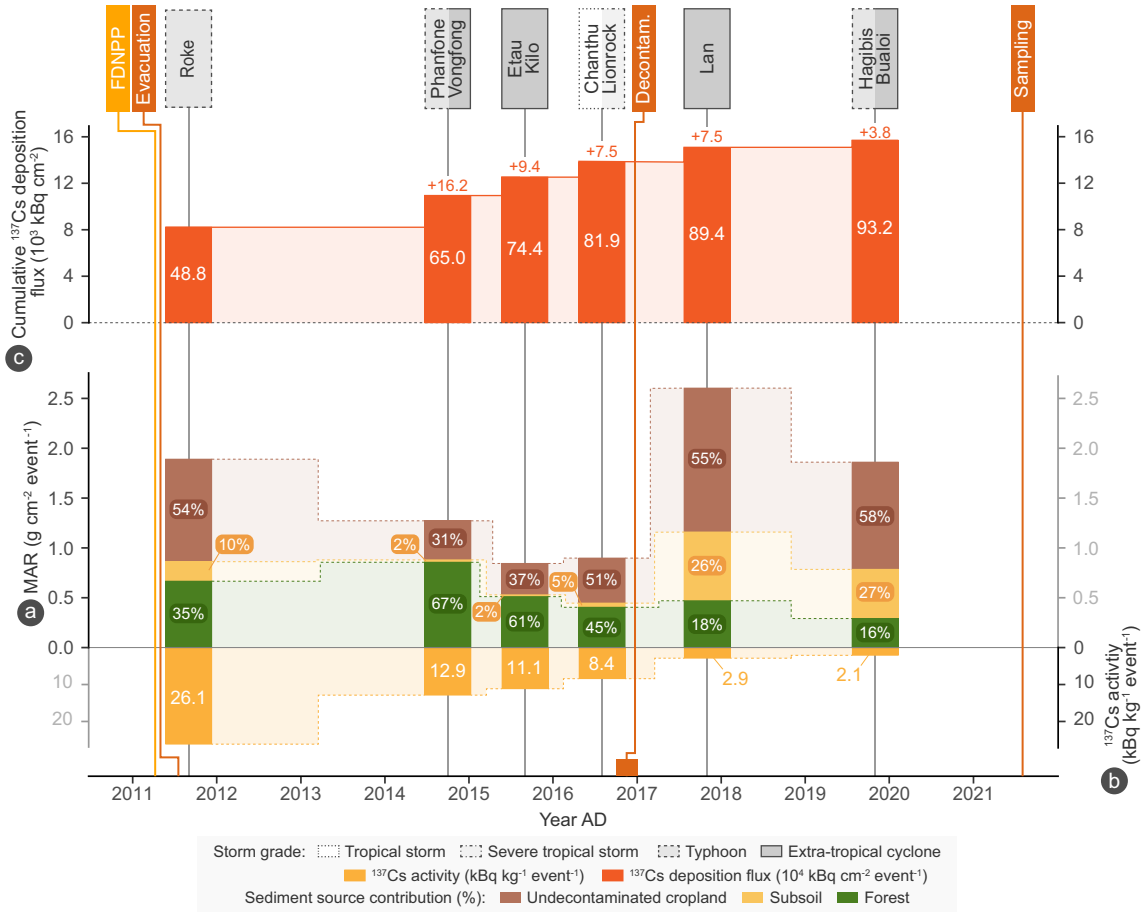

Fig. 8. Evolution of the (a) mass accumulation rate (MAR) as a function of the contribution of each sedimentary source (%), ^{137}Cs (b) activity and (c) cumulative deposition flux per extreme precipitation event identified along the sediment core sampled in the downstream part of the Mano Dam reservoir.

7.5 10^3 *kBq* m^{-2} *event*$^{-1}$). Subsequently, there was again a decrease of 49 % between 2017–2019, equivalent to a decrease of about 26 % per year. Over the period from 2011 to 2017 and 2019, ^{137}Cs deposition flux was reduced by 85 to 92 %, which was equivalent to a decrease of about 26 % per year.

Furthermore, Roke, the first extreme precipitation event that took place after FDNPP accident in 2011, accounted for 52 % of the total ^{137}Cs transferred between 2011 and 2021. The next three events, in 2014, 2015, and 2016, accounted for 18 %, 10 %, 8 % of the total ^{137}Cs transferred. Accordingly, these four events supplied 88 % of the total ^{137}Cs deposition flux exported during the monitored period. In contrast, the last two events, in 2017 and 2019, transferred a limited deposition flux of ^{137}Cs with only 8 % and 4 %, respectively.

4. Discussion

4.1. Identifying and dating sedimentation events along the sediment core

In this study, insights from Huon et al. (2018) research were used to identify sediment deposition associated with extreme precipitation events based on specific changes in the sediment properties. In addition, as most of the sediment transfer in river occurred during extreme precipitation events (Laceby et al., 2016a; Osawa et al., 2018; Taniguchi et al., 2019; Evrard et al., 2020), deposits were assumed to correspond to a succession of distinct events. However, despite the fine sampling resolution at a thickness of 1-*cm*, some of the changes occurred within this 1 *cm* interval and were smoothed out. For example, in layers at 9–11, 16–18, 19–21 and 26 – 27 *cm* depths, the decrease in SSA coincided with an increase in TOC and particle size (i.e. D90) and occurred slightly before the decrease in Al content, although all these changes should have occurred simultaneously (Fig. 4.a). Such smoothing could be reduced by increasing the resolution of the analysis, such as what can be obtained using XRF core scanner (Rapuc et al., 2020) or high-resolution hyperspectral imagery (Jacq et al., 2019).

In addition, challenges were faced in the dating of the sedimentation events due to the inability to use conventional dating methods based on ^{210}Pb$_{ex}$ and ^{137}Cs. To overcome this, several types of contextual information were used, including previously published data (Huon et al., 2018), the identification of the ^{137}Cs peak related to FDNPP fallout, management of the reservoir, the progress of decontamination, in particular the addition of fresh soil, and finally the date of sampling of the current sediment core. Consequently, our dating approach relied on establishing a relative chronology based on these contextual factors. This led to inherent uncertainties in the dating process. Notably, the strong similarities in the distribution of the properties between the sediment core studied in this study and the two downstream sediment cores studied by Huon et al. (2018) (i.e., DD1 and DD2; Supplementary Materials Fig. B1), which were sampled at the same location in the reservoir, supports a high repeatability and representativeness of sediment core sampling at this location in the reservoir. However, investigation of additional sediment cores would provide confirmation of the results.

Moreover, water level management at the Mano Dam likely impacted sedimentation in the reservoir. Adjustments of water outflow to maintain usual water levels changed the water velocity along the reservoir. Increased water release elevates water velocity, reducing the residence time of sediment-laden water, which reduces the sediment trapping

potential within the reservoir. During higher-magnitude events, such as Etau-Kilo (2015) and Hagibis & Bualoi (2019), water discharges were significantly higher during a shorter period of time compared to what was observed during lower-magnitude events (e.g. Roke (2011), Phanfone & Vongfong (2014), Chanthu & Lionrock (2016) and Lan (2017)) (Fig. 3). This fast and abrupt management pattern during higher-magnitude events was less favourable for sediment trapping than the gradual and smoother management observed for lower-magnitude events. Despite the fact that these events generated massive erosion, as observed in the suspended sediment flux records at the reservoir inlet monitoring station (Fig. 3.d) and in other studies (Thothong et al., 2011; Chartin et al., 2017; Evrard et al., 2019b; Vandromme et al., 2023), the management of the water reservoir likely resulted in a lower representation of this type of event in the lake sediment records. Conversely, the 2017 event, Lan, which occurred after decontamination and was equivalent to the Phanfone & Vongfong events (2014) in terms of precipitation, was associated with significantly higher suspended sediment flux although not with higher dam water discharge. Accordingly, this management was likely to trap more sediments in the water reservoir. The Chanthu & Lionrock events events (2016), both lower-magnitude events that occurred over a short period of time, resulted in a slightly higher water discharge than Lan (2017) or Phanfone & Vongfong (2014) events. Unexpectedly, the extreme precipitation event of September 2020 (Dolphin - 2012) did not generate significant sediment transfer (Fig. 3.d), despite having similar maximum daily precipitation as events such as Chanthu & Lionrock (2014), Phanfone & Vongfong (2016), or Lan (2017) (Supplementary Materials Table B3). The Dolphin event (2020) was not identified in the sediment core, which could be due to the resolution of the sediment core analyses (i.e. 1 *cm*) and a low amount of sediment deposition. Understanding the complex influence of these types of short-term management of water discharge and reservoir water level on sediment dynamics across the reservoir, would require the development and use of 3D water-sediment dynamics models, which could be developed in further studies. In addition, it may be possible to quantify the sediment trapping efficiency of the reservoir by comparing suspended sediment fluxes at the inlet and outlet of the reservoir (Verstraeten and Poesen, 2000).

Dam water level management types likely control the potential trapping of sediment particles in the lacustrine zone of the reservoir, in particular for the coarse particles that usually settle down first (i.e. coarse organic matter). Therefore, the occurrence of large water discharges over a short period of time may lead to a lower trapping of sediments and therefore to a lower representation of the contribution sources. However, according to Vandromme et al. (2023), the most intense events can generate rill (or gully) erosion that mobilizes subsoils, depleted in organic matter. The signature of these higher-magnitude events was therefore likely to be depleted in coarser organic matter particles, resulting in a higher contribution of sediment originating from subsoil compartments. Unlike natural lakes, managed water reservoirs do not show homogeneous sedimentation conditions throughout time, in particular in areas subject to heavy precipitation events, such as typhoons, which require rapid and major dam water releases to prevent damages to the dam structure and any flooding downstream, thereby modify the sedimentation conditions and sedimentation events signature across the reservoir.

4.2. Evolution of sediment source contributions and ^{137}TEXTCs transfers through time

Although the contrasted extreme precipitation events, all land use changes in the Mano Dam reservoir catchment have occurred over a relatively short period of ten years have been responsible for significant changes in terms of trends in the sediment source contribution. Soon after the abandonment of agricultural activities, between 2011 and 2016, the spontaneous regrowth of vegetation has progressively protected the soil from erosion and reduced the contribution of agricultural land to sediment and particle-bound ^{137}Cs transfer, as deposition flux decreased over time. Conversely, the decontamination, which mainly took place over a three-month period at the end of 2016 has drastically increased erosion of the cultivated land by leaving the soil uncovered by vegetation and/or covered with a fresh soil making it highly susceptible to erosion (Evrard et al., 2019a). As also shown by Feng et al. (2022), this effect appears to be pluriannual, as it was still visible in Mano Dam reservoir during Hagibis in 2019. However, even if these fresh soils were more sensitive to erosion, they did not provide ^{137}Cs contaminated sediments. In fact, they acted as diluents for contaminated ^{137}Cs sediment originating from undecontaminated forests, as shown by Vandromme et al. (2023). This may raise concerns about soil conservation in the decontaminated farmland. Nevertheless, due to the impact of dam water level management on sediment storage, it was likely that some intense events were not fully recorded in the sedimentation sequence. Therefore, not all the sediment and ^{137}Cs transfer episodes that occurred in the catchment were likely to be fully represented in this study. In addition, according to Funaki et al. (2022), under anoxic conditions ^{137}Cs elutes in the pore water, which may cause migration within the sediment column over time, as observed between layers F and G (Fig. 2.e and i). Although this phenomenon appears to be limited according to Funaki et al. (2022), the ^{137}Cs stock of a sedimentation event could be slightly modified after a prolonged period.

The initial intention of the sediment fingerprinting approach was to adjust the potential cropland sources as decontamination progressed (uncontaminated, decontaminated, remediated). However, it was not possible to distinguish certain sources, such as subsoil and the fresh soil added to remediated cropland, which did not allow tracing each source individually. In addition, in contrast with decontamination records no detailed spatial and/or temporal information was found on the progress of the preparation for recultivation. Moreover, due to the limitations in the Bayesian models (i.e. MixSIAR and BMM) that appear not to handle missing sources correctly Stock et al. (2018) and recommendations to limit the number of potential sources considered ($\leq$ 4, Lees (1997)), it was decided to use three well-defined sources (undecontaminated cropland, forest, subsoil).

The use of a multiple-modeling approach allowed to slightly improve the values of the evaluation metrics compared to those obtained with independent models (MixSIAR and BMM). Although multiple-modeling metrics generally exceeded those of individual models, they remained higher on average. In addition, comparing the trends obtained with individual models, which show some consistency, increased our confidence in the modeling outputs. Future studies could incorporate additional unmixing models to further improve the multi-modeling approach. Investigation of the transferability of modeling metrics from virtual mixtures to actual sediment samples, using ESP values, did not support a high confidence in the transferability of the metrics in the current context. This was probably attributed to the selection of tracers with non-(fully) conservative behaviour, which was reproduced in the generation of the virtual mixtures (Chalaux-Clergue et al., 2024a).

4.3. Perspectives and management implications

Previous studies showed a strong decrease in the ^{137}Cs activities in sediment over time (Osawa et al., 2018; Taniguchi et al., 2019; Evrard et al., 2020). Prior to the decontamination, this reduction in ^{137}Cs activity was associated to both physical decay and prior lateral transfer in rivers. After decontamination, previous studies associated the significant decrease in ^{137}Cs activity with the removal of contaminated soils or the physical decay that reduced ^{137}Cs fluxes. However, the current results suggest that it was more likely to be related to the dilution of contaminated sediment with fresh soil spread over decontaminated farmland, rather than a decrease in ^{137}Cs deposition fluxes. The natural regrowth of spontaneous vegetation over farmland since 2011 until decontamination has gradually reduced soil erosion, decreasing the

contribution of this source to sediment and particle-bound ^{137}Cs transfer in rivers (Feng et al., 2022). Here, decontamination appeared to have achieved a similar or slightly better reduction than natural regrowth, by removing contaminated erodible soil.

Nevertheless, as observed along the sediment core, the forest has consistently contributed sediment and particle-bound ^{137}Cs and while remaining the main source of ^{137}Cs in the catchment (Laceby et al., 2016b). The resumption of agricultural activities on decontaminated soil, associated with a denser vegetation cover, may further reduce erosion from cropland. Therefore, this will likely reduce the supply of sediment depleted in radiocesium, which may reduce the dilution of that of forest - enriched in radiocesium -, leading to a potential future increase of sediment ^{137}Cs activity. However, over time, ^{137}Cs tends to migrate into forest soils and becomes increasingly immobilised by clay minerals (Kurikami et al., 2019; Onda et al., 2020). Moreover, Taira et al. (2020) showed that ^{137}Cs activity in forest soils was not modified by the occurrence of extreme precipitation events, as they mainly induce rill erosion mainly transferring material depleted in radiocesium (Vandromme et al., 2023). This could potentially lead to a reduction in radiocesium-rich sediment originating from forests.

This being said, the primary objective of the decontamination was to reduce the ambient air dose rate, which proved to be successful (Evrard et al., 2019b). In farmland, the ambient air dose rate was reduced by an average of about 59 %, reaching 0.59 $\mu Sv\, h^{-1}$ (MoE, 2018, 2023b). This level remains above the long term target ambient air dose rate of 0.23 $\mu Sv\, h^{-1}$ (equivalent to an exposure dose rate of 1 $mSv\, yr^{-1}$), although it allows the resumption of agricultural activities. However, in contrast with conclusions of previous studies, our current research emphasises that decontamination may not have reduced the deposition flux of particle-bound ^{137}Cs in the reservoir transferred by erosion in rivers as much as it was often previously assumed. This finding is supported by a modeling approach conducted by Vandromme et al. (2023), demonstrating a 17 % reduction in ^{137}Cs flux in rivers compared to scenarios without decontamination. Decontamination resulted in a similar ^{137}Cs deposition flux as that observed in landscapes characterised by a dense vegetation regrowth, such as that which developed during the early post-accidental period when farmlands were abandoned. This raises the question of the worthiness of decontamination in terms of reduction in particulate transfers in rivers, considering the workload, cost and quantity of waste generated by the remediation (Evrard et al., 2023). However, decontamination - through reducing the ambient air dose rate in residential and agricultural areas - theoretically allows the population to return. Nevertheless, according to Asanuma-Brice et al. (2023), very few people have returned or moved to these areas. This is related to the deterioration and modification of living conditions in comparison with pre-accidental conditions (e.g. dislocation of families and neighbourhood relations, lack of facilities, public services and economic activities, transformation of the landscape, restricted access to forest by-products such as gathering wild vegetables or mushrooms).

Nevertheless, if the objective is to allow a rapid return of the population and to limit riverine transfers of radioactive contamination, as intended by the Japanese government, our current results suggest that further reducing the delay between the accident and the decontamination could have reduced ^{137}Cs transfers in rivers more effectively. Therefore, an earlier implementation of farmland decontamination within 4–5 years after an accident could have led to a more effective reduction of transfers. This recommendation is consistent with similar findings obtained in forests, where it was shown that decontamination within 1 to 5-years after the accident would be more effective (Thiry et al., 2018; Koarashi et al., 2020). The validity of this recommendation could be further tested by studying catchments decontaminated over different timescales (relatively early or later after the accident).

5. Conclusions

Through a combination of analyses of the Mano Dam reservoir sediment core properties (organic matter, elemental geochemistry, visible colourimetry, and granulometry) coupled with contextual information (previous study of Huon et al. (2018), daily precipitation records, dam water level management, progress of decontamination), sedimentation events of the last decade were identified and dated despite the impossibility of using a more conventional dating approach. In total, six major events were identified between the FDNPP accident in March 2011 and the core sampling campaign in June 2021. Among these events, four occurred before the completion of decontamination at the end of 2016 and two thereafter.

The study revealed significant modifications in sediment source contributions over the last decade following FDNPP accident, mainly driven by rapid and drastic changes in land uses. During the period of abandonment of agricultural activities in response to the evacuation order, the quantitative contribution of cropland gradually decreased (by about 27 % of the pre-accidental level). Furthermore, a decrease in both ^{137}Cs activity in the sediment (by about 67 % equivalent to 19% yr^{-1}) and ^{137}Cs deposition flux per extreme precipitation event (by about 84 %) was observed during these five years, between 2011 and 2016. In contrast, after decontamination, cropland and added fresh soil excessively contributed to sediment transfer. Meanwhile, forests that have not been decontaminated, appeared to supply a stable and perennial source of ^{137}Cs-contaminated sediment. Therefore, by providing non-contaminated sediment, decontaminated cropland and fresh soil contributed to the dilution of ^{137}Cs borne by contaminated sediment, resulting in an overall drop of ^{137}Cs activity in the sediment (by 65 % between 2016 and 2017). However, this was not associated with a reduction in the ^{137}Cs deposition flux, as forested areas act a stable source of ^{137}Cs-contaminated sediment. Accordingly, the resulting ^{137}Cs deposition flux after decontamination (2016–2021) was similar to that observed during the 5-year period of land abandonment (2011–2016), as a result of the natural regrowth of spontaneous vegetation over farmland, which protected soils and limited ^{137}Cs transfer by rivers.

Future studies should investigate other catchments of the Fukushima region that have been decontaminated later than the Mano Dam reservoir catchment, or that have not been decontaminated yet, to assess the effect of longer land abandonment periods on ^{137}Cs fluxes in rivers.

Financial support

The collection and the analysis of the soil and sediment samples were funded by the TOFU (ANR-11-JAPN-001) and the AMORAD (ANR-11-RSNR-0002) projects, under the supervision of the French National Research Agency (ANR, Agence Nationale de la Recherche). The support of CEA (Commissariat à l'Energie Atomique et aux Energies Alternatives, France), CNRS (Centre National de la Recherche Scientifique, France) and JSPS (Japan Society for the Promotion of Science) through the funding of PhD fellowships (Hugo Lepage, Hugo Jaegler, Thomas Chalaux-Clergue) and collaboration projects (grant no. PRC CNRS JSPS 2019-2020, no.10; CNRS International Research Project – IRP – MITATE Lab) is recognised. Thomas Chalaux-Clergue obtained a JSPS grant to spend the second year of his PhD at Kyoto Prefectural University (Oct. 2022 - Sept. 2023) (Grant number PE22708). This work was also supported by ERAN (Environmental Radioactivity Research Network Center) (grants I-21-22 and I-22-24) and a mini-project from the FIRE (Fédération Ile-de-France de Recherche en Environnement - CNRS FR3020 FIRE, France) entitled RICOR ('Reconstructing the Impact of Changing land Occupation on the fate of Radionuclides').

CRediT authorship contribution statement

Thomas Chalaux-Clergue: Writing – original draft, Visualization,

Software, Methodology, Investigation, Formal analysis, Data curation, Conceptualization. **Anthony Foucher:** Writing – review & editing, Methodology, Conceptualization. **Pierre-Alexis Chaboche:** Writing – review & editing. **Seiji Hayashi:** Writing – review & editing, Resources, Investigation. **Hideki Tsuji:** Writing – review & editing, Resources, Investigation. **Yoshifumi Wakiyama:** Writing – review & editing, Resources, Investigation. **Sylvain Huon:** Writing – review & editing, Investigation. **Rosalie Vandromme:** Writing – review & editing. **Atsushi Nakao:** Writing – review & editing, Supervision. **Olivier Evrard:** Writing – review & editing, Supervision, Project administration, Investigation, Funding acquisition, Data curation, Conceptualization.

Declaration of competing interest

Olivier Evrard reports financial support was provided by French National Research Agency. Olivier Evrard reports financial support was provided by French Alternative Energies and Atomic Energy Commission (CEA). Olivier Evrard reports financial support was provided by French National Center for Scientific Research (CNRS). Thomas Chalaux-Clergue reports financial support was provided by French Alternative Energies and Atomic Energy Commission. Thomas Chalaux-Clergue reports financial support was provided by Japan Society for the Promotion of Science (JSPS). Olivier Evrard reports financial support was provided by Environmental Radioactivity Research Network Center (ERAN). If there are other authors, they declare that they have no known competing financial interests or personal relationships that could have appeared to influence the work reported in this paper.

Data availability

The dataset is available online at https://zenodo.org/records/10836974 (Chalaux-Clergue et al., 2024b). The code to run models, summarise results and plot results is available in the Supplement (.Rmd file).

Acknowledgements

The assistance provided by Dr. H. Funaki and Dr. K. Yoshimura from the Japan Atomic Energy Agency) in conducting the sediment core sampling in the Mano Dam reservoir is gratefully acknowledged.

This research was funded, in part, by the French National Research Agency (ANR, Agence Nationale de la Recherche). A CC-BY public copyright license has been applied by the authors to the present document and will be applied to all subsequent versions up to the Author Accepted Manuscript arising from this submission, in accordance with the grant's open access conditions.

Appendix A. Supplementary data

Supplementary data to this article can be found online at https://doi.org/10.1016/j.scitotenv.2024.174546.

References

Amorim, H.C., Hurtarte, L.C., Souza, I.F., Zinn, Y.L., 2022. C:N ratios of bulk soils and particle-size fractions: global trends and major drivers. Geoderma 425, 116026. https://linkinghub.elsevier.com/retrieve/pii/S0016706122003330. https://doi.org/10.1016/j.geoderma.2022.116026.

Asanuma-Brice, C., Evrard, O., Chalaux, T., 2023. Why did so few refugees return to the Fukushima fallout-impacted region after remediation? An interdisciplinary case study from litate village, Japan. Int. J. Disaster Risk Reduction 85, 103498. URL: https://linkinghub.elsevier.com/retrieve/pii/S2212420922007178 https://doi.org/10.1016/j.ijdrr.2022.103498.

Batista, P.V.G., Laceby, J.P., Silva, M.L.N., Tassinari, D., Bispo, D.F.A., Curi, N., Davies, J., Quinton, J.N., 2019. Using pedological knowledge to improve sediment source apportionment in tropical environments. J. Soil. Sediment. 19, 3274–3289. URL: http://link.springer.com/10.1007/s11368-018-2199-5 https://doi.org/10.1007/s11368-018-2199-5.

Batista, P.V.G., Laceby, J.P., Evrard, O., 2022. How to evaluate sediment fingerprinting source apportionments. J. Soil. Sediment. 22, 1315–1328. https://link.springer.com/10.1007/s11368-022-03157-4. https://doi.org/10.1007/s11368-022-03157-4.

Beck, H.E., Zimmermann, N.E., McVicar, T.R., Vergopolan, N., Berg, A., Wood, E.F., 2018. Present and future Köppen-Geiger climate classification maps at 1-km resolution. Sci. Data 5, 180214. http://www.nature.com/articles/sdata2018214. https://doi.org/10.1038/sdata.2018.214.

Bruni, E., Chenu, C., Abramoff, R.Z., Baldoni, G., Barkusky, D., Clivot, H., Huang, Y., Kätterer, T., Pikuła, D., Spiegel, H., Virto, I., Guenet, B., 2022. Multi-modelling predictions show high uncertainty of required carbon input changes to reach a 4‰ target. Eur. J. Soil Sci. 73, e13330. URL: https://bsssjournals.onlinelibrary.wiley.com/doi/10.1111/ejss.13330 https://doi.org/10.1111/ejss.13330.

Cao, L., Ishii, N., Zheng, J., Kagami, M., Pan, S., Tagami, K., Uchida, S., 2017. Vertical distributions of Pu and radiocesium isotopes in sediments from Lake Inba after the Fukushima Daiichi nuclear power plant accident: source identification and accumulation. Appl. Geochem. 78, 287–294. https://linkinghub.elsevier.com/retrieve/pii/S0883292716303651. https://doi.org/10.1016/j.apgeochem.2017.01.012.

Chalaux-Clergue, T., Bizeul, R.. fingR: A Support for Sediment Source Fingerprinting Studies. URL. https://github.com/tchalauxclergue/fingR.

Chalaux-Clergue, T., Bizeul, R., Batista, P.V.G., Martínez-Carreras, N., Laceby, J.P., Evrard, O., 2024a. Sensitivity of source sediment fingerprinting to tracer selection methods. SOIL 10, 109–138. https://soil.copernicus.org/articles/10/109/2024/. https://doi.org/10.5194/soil-10-109-2024.

Chalaux-Clergue, T., Evrard, O., Durand, R., Caumon, A., Hayashi, S., Tsuji, H., Huon, S., Vaury, V., Wakiyama, Y., Nakao, A., Laceby, J.P., Onda, Y.. Organic Matter, Geochemical, Visible Spectrocolorimetric Properties, Radiocesium Properties, and Grain Size of Potential Source Material, Target Sediment Core Layers and Laboratory Mixtures for Conducting Sediment Fingerprinting Approaches in the Mano Dam Reservoir (Hayama Lake) Catchment, Fukushima Prefecture, Japan. https://zenodo.org/records/10836974.

Chartin, C., Evrard, O., Onda, Y., Patin, J., Lefèvre, I., Ottlé, C., Ayrault, S., Lepage, H., Bonté, P., 2013. Tracking the early dispersion of contaminated sediment along rivers draining the Fukushima radioactive pollution plume. Anthropocene 1, 23–34. https://doi.org/10.1016/j.ancene.2013.07.001. https://linkinghub.elsevier.com/retrieve/pii/S2213305413000088.

Chartin, C., Evrard, O., Laceby, J.P., Onda, Y., Ottlé, C., Lefèvre, I., Cerdan, O., 2017. The impact of typhoons on sediment connectivity: lessons learnt from contaminated coastal catchments of the Fukushima Prefecture (Japan): typhoon impact on sediment connectivity - Fukushima, Japan. Earth Surf. Process. Landf. 42, 306–317. https://onlinelibrary.wiley.com/doi/10.1002/esp.4056. https://doi.org/10.1002/esp.4056.

Chino, M., Nakayama, H., Nagai, H., Terada, H., Katata, G., Yamazawa, H., 2011. Preliminary estimation of release amounts of 131 I and 137 Cs accidentally discharged from the Fukushima Daiichi nuclear power plant into the atmosphere. J. Nucl. Sci. Technol. 48, 1129–1134. http://www.tandfonline.com/doi/abs/10.1080/18811248.2011.9711799. https://doi.org/10.1080/18811248.2011.9711799.

Debret, M., Sebag, D., Desmet, M., Balsam, W., Copard, Y., Mourier, B., Susperrigui, A.S., Arnaud, F., Bentaleb, I., Chapron, E., Lallier-Vergès, E., Winiarski, T., 2011. Spectrocolorimetric interpretation of sedimentary dynamics: the new "Q7/4 diagram". Earth Sci. Rev. 109, 1–19. URL: https://linkinghub.elsevier.com/retrieve/pii/S0012825211000985 https://doi.org/10.1016/j.earscirev.2011.07.002.

Duan, H., Zhang, G., Wang, S., Fan, Y., 2019. Robust climate change research: a review on multi-model analysis. Environ. Res. Lett. 14, 033001. URL: https://iopscience.iop.org/article/10.1088/1748-9326/aaf8f9 https://doi.org/10.1088/1748-9326/aaf8f9.

Evrard, O., Chartin, C., Onda, Y., Lepage, H., Cerdan, O., Lefèvre, I., Ayrault, S., 2014. Renewed soil erosion and remobilisation of radioactive sediment in Fukushima coastal rivers after the 2013 typhoons. Sci. Rep. 4, 4574. URL: https://www.nature.com/articles/srep04574 https://doi.org/10.1038/srep04574.

Evrard, O., Laceby, J.P., Lepage, H., Onda, Y., Cerdan, O., Ayrault, S., 2015. Radiocesium transfer from hillslopes to the Pacific Ocean after the Fukushima nuclear power plant accident: a review. J. Environ. Radioact. 148, 92–110. https://linkinghub.elsevier.com/retrieve/pii/S0265931X1530031X. https://doi.org/10.1016/j.jenvrad.2015.06.018.

Evrard, O., Laceby, J.P., Onda, Y., Wakiyama, Y., Jaegler, H., Lefèvre, I., 2016. Quantifying the dilution of the radiocesium contamination in Fukushima coastal river sediment (2011–2015). Sci. Rep. 6, 34828. URL: https://www.nature.com/articles/srep34828 https://doi.org/10.1038/srep34828.

Evrard, O., Durand, R., Foucher, A., Tiecher, T., Sellier, V., Onda, Y., Lefèvre, I., Cerdan, O., Laceby, J.P., 2019a. Using spectrocolourimetry to trace sediment source dynamics in coastal catchments draining the main Fukushima radioactive pollution plume (2011–2017). J. Soil. Sediment. 19, 3290–3301. http://link.springer.com/10.1007/s11368-019-02302-w. https://doi.org/10.1007/s11368-019-02302-w.

Evrard, O., Laceby, J.P., Nakao, A., 2019b. Effectiveness of landscape decontamination following the Fukushima nuclear accident: a review. SOIL 5, 333–350. https://soil.copernicus.org/articles/5/333/2019/. https://doi.org/10.5194/soil-5-333-2019.

Evrard, O., Durand, R., Nakao, A., Laceby, P.J., Lefèvre, I., Wakiyama, Y., Hayashi, S., Asanuma-Brice, C., Cerdan, O., 2020. Impact of the 2019 typhoons on sediment source contributions and radiocesium concentrations in rivers draining the Fukushima radioactive plume, Japan. Comptes Rendus. Géoscience 352, 199–211. https://comptes-rendus.academie-sciences.fr/geoscience/item/CRGEOS_2020__352_3_199_0. https://doi.org/10.5802/crgeos.42.

Evrard, O., Chalaux-Clergue, T., Chaboche, P.A., Wakiyama, Y., Thiry, Y., 2023. Research and management challenges following soil and landscape decontamination at the onset of the reopening of the Difficult-To-Return Zone, Fukushima (Japan). SOIL 9, 479–497. https://soil.copernicus.org/articles/9/479/2023/. https://doi.org/10.5194/soil-9-479-2023.

Feng, B., Onda, Y., Wakiyama, Y., Taniguchi, K., Hashimoto, A., Zhang, Y., 2022. Persistent impact of Fukushima decontamination on soil erosion and suspended sediment. Nat. Sustain. https://doi.org/10.1038/s41893-022-00924-6. URL: https://www.nature.com/articles/s41893-022-00924-6.

Foucher, A., Tassano, M., Chaboche, P.A., Chalar, G., Cabrera, M., Gonzalez, J., Cabral, P., Simon, A.C., Agelou, M., Ramon, R., Tiecher, T., Evrard, O., 2023. Inexorable land degradation due to agriculture expansion in South American Pampa. Nat. Sustain. 6, 662–670. https://www.nature.com/articles/s41893-023-01074-z. https://doi.org/10.1038/s41893-023-01074-z.

Fukushima Prefecture. Management of the Mano dam reservoir water level. https://kaseninf.pref.fukushima.jp/.

Fukuyama, T., Onda, Y., Gomi, T., Yamamoto, K., Kondo, N., Miyata, S., Kosugi, K., Mizugaki, S., Tsubonuma, N., 2010. Quantifying the impact of forest management practice on the runoff of the surface-derived suspended sediment using fallout radionuclides. Hydrol. Process. 24, 596–607. https://onlinelibrary.wiley.com/doi/10.1002/hyp.7554. https://doi.org/10.1002/hyp.7554.

Funaki, H., Tsuji, H., Nakanishi, T., Yoshimura, K., Sakuma, K., Hayashi, S., 2022. Remobilisation of radiocaesium from bottom sediments to water column in reservoirs in Fukushima, Japan. Sci. Total Environ. 812, 152534. URL: https://linkinghub.elsevier.com/retrieve/pii/S0048969721076129 https://doi.org/10.1016/j.scitotenv.2021.152534.

Guo, Z., Dirmeyer, P.A., Gao, X., Zhao, M., 2007. Improving the quality of simulated soil moisture with a multi-model ensemble approach. Q. J. Roy. Meteorol. Soc. 133, 731–747. https://onlinelibrary.wiley.com/doi/10.1002/qj.48. https://doi.org/10.1002/qj.48.

Hashimoto, S., Ugawa, S., Nanko, K., Shichi, K., 2012. The total amounts of radioactively contaminated materials in forests in Fukushima, Japan. Sci. Rep. 2, 416. https://www.nature.com/articles/srep00416. https://doi.org/10.1038/srep00416.

Hayashi, S., Hideki, T., Vandromme, R., Evrard, O., Grangeon, T., Landemaine, V., Laceby, J.P., Wakiyama, Y., Cerdan, O.. River Monitoring, Particulate Cs-137 Measurements and Rainfall Monintoring of the Mano Dam Catchment (Japan) from 2014 to 2019. URL. https://zenodo.org/record/7886523.

He, Q., Walling, D., 1996. Interpreting particle size effects in the adsorption of 137Cs and unsupported 210Pb by mineral soils and sediments. J. Environ. Radioact. 30, 117–137. https://linkinghub.elsevier.com/retrieve/pii/0265931X96892757. https://doi.org/10.1016/0265-931X(96)89275-7.

Huon, S., Hayashi, S., Laceby, J.P., Tsuji, H., Onda, Y., Evrard, O., 2018. Source dynamics of radiocesium-contaminated particulate matter deposited in an agricultural water reservoir after the Fukushima nuclear accident. Sci. Total Environ. 612, 1079–1090. https://linkinghub.elsevier.com/retrieve/pii/S0048969717319083. https://doi.org/10.1016/j.scitotenv.2017.07.205.

Iwagami, S., Onda, Y., Tsujimura, M., Abe, Y., 2017. Contribution of radioactive 137Cs discharge by suspended sediment, coarse organic matter, and dissolved fraction from a headwater catchment in Fukushima after the Fukushima Dai-ichi nuclear power plant accident. J. Environ. Radioact. 166, 466–474. https://linkinghub.elsevier.com/retrieve/pii/S0265931X16302557. https://doi.org/10.1016/j.jenvrad.2016.07.025.

Jacq, K., Perrette, Y., Fanget, B., Sabatier, P., Coquin, D., Martinez-Lamas, R., Debret, M., Arnaud, F., 2019. High-resolution prediction of organic matter concentration with hyperspectral imaging on a sediment core. Sci. Total Environ. 663, 236–244. https://linkinghub.elsevier.com/retrieve/pii/S0048969719303699. https://doi.org/10.1016/j.scitotenv.2019.01.320.

JAXA, 2016. High-resolution land-use and land-cover map of Japan [2006 ~ 2011] (ver. 16.09; 10-m resolution; 12 categories). https://www.eorc.jaxa.jp/ALOS/en/dataset/lulc/lulc_jpn_e.htm.

JAXA, 2018. High-resolution land-use and land-cover map of Japan [2014 ~ 2016] (ver. 18.03; 30-m resolution; 12 categories). https://www.eorc.jaxa.jp/ALOS/en/dataset/lulc/lulc_v1803_e.htm.

JAXA, 2022. High-resolution land-use and land-cover map of Japan [2018 ~ 2020] (ver. 21.11; 10-m resolution; 12 categories). https://www.eorc.jaxa.jp/ALOS/en/dataset/lulc/lulc_v2111_e.htm.

JMA, 2023. Historical weather data and download from all over Japan. URL. https://www.jma.go.jp/jma/jma-eng/jma-center/rsmc-hp-pub-eg/RSMC_HP.htm.

Kato, H., Onda, Y., Teramage, M., 2012. Depth distribution of 137Cs, 134Cs, and 131I in soil profile after Fukushima Dai-ichi nuclear power plant accident. J. Environ. Radioact. 111, 59–64. https://linkinghub.elsevier.com/retrieve/pii/S0265931X11002426. https://doi.org/10.1016/j.jenvrad.2011.10.003.

Kato, H., Onda, Y., Gao, X., Sanada, Y., Saito, K., 2019. Reconstruction of a Fukushima accident-derived radiocesium fallout map for environmental transfer studies. J. Environ. Radioact. 210, 105996. https://linkinghub.elsevier.com/retrieve/pii/S0265931X18303308. https://doi.org/10.1016/j.jenvrad.2019.105996.

Kitamura, A., Kurikami, H., Sakuma, K., Malins, A., Okumura, M., Machida, M., Mori, K., Tada, K., Tawara, Y., Kobayashi, T., Yoshida, T., Tosaka, H., 2016. Redistribution and export of contaminated sediment within eastern Fukushima Prefecture due to typhoon flooding: redistribution and export of contaminated sediment. Earth Surf. Process. Landf. 41, 1708–1726. https://onlinelibrary.wiley.com/doi/10.1002/esp.3944. https://doi.org/10.1002/esp.3944.

Knudson, C., Vats, D., 2022. StaleGR: A Stable Gelman-Rubin Diagnostic for Markov Chain Monte Carlo. URL. https://cran.r-project.org/web/packages/stableGR/index.html.

Koarashi, J., Atarashi-Andoh, M., Nishimura, S., Muto, K., 2020. Effectiveness of decontamination by litter removal in Japanese forest ecosystems affected by the Fukushima nuclear accident. Sci. Rep. 10, 6614. URL: https://www.nature.com/articles/s41598-020-63520-8 https://doi.org/10.1038/s41598-020-63520-8.

Kobayashi, T., Nagai, H., Chino, M., Kawamura, H., 2013. Source term estimation of atmospheric release due to the Fukushima Dai-ichi Nuclear Power Plant accident by atmospheric and oceanic dispersion simulations: Fukushima NPP accident related. J. Nuclear Sci. Technol. 50, 255–264. http://www.tandfonline.com/doi/abs/10.1080/00223131.2013.772449. https://doi.org/10.1080/00223131.2013.772449.

Konoplev, A., Golosov, V., Wakiyama, Y., Takase, T., Yoschenko, V., Yoshihara, T., Parenyuk, O., Cresswell, A., Ivanov, M., Carradine, M., Nanba, K., Onda, Y., 2018. Natural attenuation of Fukushima-derived radiocesium in soils due to its vertical and lateral migration. J. Environ. Radioact. 186, 23–33. https://linkinghub.elsevier.com/retrieve/pii/S0265931X17303296. https://doi.org/10.1016/j.jenvrad.2017.06.019.

Konoplev, A., Wakiyama, Y., Wada, T., Ivanov, M., Komissarov, M., Nanba, K., 2022. Reconstruction of time changes in radiocesium concentrations in the river of the Fukushima Dai-ichi NPP contaminated area based on its depth distribution in dam reservoir's bottom sediments. Environ. Res. 206, 112307. https://linkinghub.elsevier.com/retrieve/pii/S001393512101608X. https://doi.org/10.1016/j.envres.2021.112307.

Kurikami, H., Sakuma, K., Malins, A., Sasaki, Y., Niizato, T., 2019. Numerical study of transport pathways of 137Cs from forests to freshwater fish living in mountain streams in Fukushima, Japan. J. Environ. Radioact. 208–209, 106005. https://linkinghub.elsevier.com/retrieve/pii/S0265931X18308853. https://doi.org/10.1016/j.jenvrad.2019.106005.

Laceby, J.P., Chartin, C., Evrard, O., Onda, Y., Garcia-Sanchez, L., Cerdan, O., 2016a. Rainfall erosivity in catchments contaminated with fallout from the Fukushima Daiichi nuclear power plant accident. Hydrol. Earth Syst. Sci. 20, 2467–2482. URL: https://hess.copernicus.org/articles/20/2467/2016/ https://doi.org/10.5194/hess-20-2467-2016.

Laceby, J.P., Huon, S., Onda, Y., Vaury, V., Evrard, O., 2016b. Do forests represent a long-term source of contaminated particulate matter in the Fukushima Prefecture? J. Environ. Manage. 183, 742–753. https://linkinghub.elsevier.com/retrieve/pii/S0301479716306661. https://doi.org/10.1016/j.jenvman.2016.09.020.

Lal, R., 2001. Soil degradation by erosion. Land Degrad. Dev. 12, 519–539. https://onlinelibrary.wiley.com/doi/10.1002/ldr.472. https://doi.org/10.1002/ldr.472.

Lamb, A.L., Wilson, G.P., Leng, M.J., 2006. A review of coastal palaeoclimate and relative sea-level reconstructions using δ13C and C/N ratios in organic material. Earth-Sci. Rev. 75, 29–57. https://linkinghub.elsevier.com/retrieve/pii/S0012825205001376. https://doi.org/10.1016/j.earscirev.2005.10.003.

Lees, J.A., 1997. Mineral magnetic properties of mixtures of environmental and synthetic materials: linear additivity and interaction effects. Geophys. J. Int. 131, 335–346. https://academic.oup.com/gji/article-lookup/doi/10.1111/j.1365-246X.1997.tb01226.x. https://doi.org/10.1111/j.1365-246X.1997.tb01226.x.

Lepage, H., Evrard, O., Onda, Y., Lefèvre, I., Laceby, J.P., Ayrault, S., 2015. Depth distribution of cesium-137 in paddy fields across the Fukushima pollution plume in 2013. J. Environ. Radioact. 147, 157–164. https://linkinghub.elsevier.com/retrieve/pii/S0265931X15001484. https://doi.org/10.1016/j.jenvrad.2015.05.003.

Lepage, H., Laceby, J.P., Bonté, P., Joron, J.L., Onda, Y., Lefèvre, I., Ayrault, S., Evrard, O., 2016. Investigating the source of radiocesium contaminated sediment in two Fukushima coastal catchments with sediment tracing techniques. Anthropocene 13, 57–68. https://linkinghub.elsevier.com/retrieve/pii/S2213305416300042. https://doi.org/10.1016/j.ancene.2016.01.004.

MoE, 2013. Decontamination Guidelines. Technical Report 2. Japanese Ministry of Environment, Japan.

MoE, 2015. Decontamination Report - A Compilation of Experiences to Date on Decontamination for the Living Environment Conducted by the Ministry of the Environment. Technical Report. Japanese Ministry of Environment, Japan. http://josen.env.go.jp/en/policy_document/.

MoE, 2018. Decontamination Projects for Radioactive Contamination Discharged by Tokyo Electric Power Company Fukushima Daiichi Nuclear Power Station Accident. Technical Report. Japanese Ministry of Environment.
MoE, 2023. Information on decontamination – Fukushima revitalisation in data. Technical Report. Japanese Ministry of Environment. http://josen.env.go.jp/plaza/info/data/pdf/data_2303_01.pdf.
MoE, 2023a. Decontamination status. URL. http://josen.env.go.jp/area/.
MoE, 2023b. Environmental Remediation. URL. http://josen.env.go.jp/en/decontamination/.
Morino, Y., Ohara, T., Watanabe, M., Hayashi, S., Nishizawa, M., 2013. Episode analysis of deposition of Radiocesium from the Fukushima Daiichi nuclear power plant accident. Environ. Sci. Technol. 47, 2314–2322. URL: https://pubs.acs.org/doi/10.1021/es304620x https://doi.org/10.1021/es304620x.
Mukundan, R., Radcliffe, D.E., Ritchie, J.C., Risse, L.M., McKinley, R.A., 2010. Sediment fingerprinting to determine the source of suspended sediment in a southern Piedmont stream. J. Environ. Qual. 39, 1328–1337. https://onlinelibrary.wiley.com/doi/10.2134/jeq2009.0405. https://doi.org/10.2134/jeq2009.0405.
Nakao, A., Ogasawara, S., Sano, O., Ito, T., Yanai, J., 2014. Radiocesium sorption in relation to clay mineralogy of paddy soils in Fukushima, Japan. Sci. Total Environ. 468–469, 523–529. URL: https://linkinghub.elsevier.com/retrieve/pii/S0048969713009893 https://doi.org/10.1016/j.scitotenv.2013.08.062.
Nakao, A., Takeda, A., Ogasawara, S., Yanai, J., Sano, O., Ito, T., 2015. Relationships between paddy soil radiocesium interception potentials and physicochemical properties in Fukushima, Japan. J. Environ. Qual. 44, 780–788. http://doi.wiley.com/10.2134/jeq2014.10.0423. https://doi.org/10.2134/jeq2014.10.0423.
Obara, H., Ohkura, T., Takata, Y., Kohyama, K., Maejima, Y., Hamazaki, T., 2011. Comprehensive soil classification system of Japan first approximation. Nogyo Kankyo Gijutsu Kenkyusho Hokoku = Bull. Natl. Inst. Agro-Environ. Sci. 1–73. http://www.niaes.affrc.go.jp/sinfo/publish/public_e.html.
Obara, H., Maejima, Y., Kohyama, K., Ohkura, T., Takata, Y., 2015. Outline of the comprehensive soil classification system of Japan – first approximation. Jpn Agric. Res. Q. 49, 217–226. https://www.jstage.jst.go.jp/article/jarq/49/3/49_217/_article. https://doi.org/10.6090/jarq.49.217.
Onda, Y., Taniguchi, K., Yoshimura, K., Kato, H., Takahashi, J., Wakiyama, Y., Coppin, F., Smith, H., 2020. Radionuclides from the Fukushima Daiichi Nuclear Power Plant in terrestrial systems. Nat. Rev. Earth Environ. 1, 644–660. https://www.nature.com/articles/s43017-020-0099-x. https://doi.org/10.1038/s43017-020-0099-x.
Osawa, K., Nonaka, Y., Nishimura, T., Tanoi, K., Matsui, H., Mizogichi, M., Tatsuno, T., 2018. Quantification of dissolved and particulate radiocesium fluxes in two rivers draining the main radioactive pollution plume in Fukushima, Japan (2013–2016). Anthropocene 22, 40–50. https://linkinghub.elsevier.com/retrieve/pii/S2213305418300262. https://doi.org/10.1016/j.ancene.2018.04.003.
Palazón, L., Latorre, B., Gaspar, L., Blake, W.H., Smith, H.G., Navas, A., 2015. Comparing catchment sediment fingerprinting procedures using an auto-evaluation approach with virtual sample mixtures. Sci. Total Environ. 532, 456–466. https://linkinghub.elsevier.com/retrieve/pii/S0048969715300619. https://doi.org/10.1016/j.scitotenv.2015.05.003.
QGIS Development Team, 2022. QGIS geographic information system. Open Source Geospatial Foundation. https://www.qgis.org/fr/site/.
R Core Team, 2022. A language and environment for statistical computing. R foundation for statistical computing. https://www.R-project.org/.
Rapuc, W., Jacq, K., Develle, A.L., Sabatier, P., Fanget, B., Perrette, Y., Coquin, D., Debret, M., Wilhelm, B., Arnaud, F., 2020. XRF and hyperspectral analyses as an automatic way to detect flood events in sediment cores. Sediment. Geol. 409, 105776. URL: https://linkinghub.elsevier.com/retrieve/pii/S0037073820301913 https://doi.org/10.1016/j.sedgeo.2020.105776.
RSMC, 2023. RSMC Typhoon Best Track Data and Graphics [2006 2021]. URL. https://www.jma.go.jp/jma/jma-eng/jma-center/rsmc-hp-pub-eg/trackarchives.html.
RSMC, 2024. Tropical Cyclone Information. URL. https://www.jma.go.jp/jma/jma-eng/jma-center/rsmc-hp-pub-eg/RSMC_HP.htm.
RStudio Team, 2023. RStudio: Integrated Development Environment for R. RStudio, URL. http://www.rstudio.com/.
Saito, T., Makino, H., Tanaka, S., 2014. Geochemical and grain-size distribution of radioactive and stable cesium in Fukushima soils: implications for their long-term behavior. J. Environ. Radioact. 138, 11–18. https://linkinghub.elsevier.com/retrieve/pii/S0265931X14002306. https://doi.org/10.1016/j.jenvrad.2014.07.025.
Sakaguchi, A., Tanaka, K., Iwatani, H., Chiga, H., Fan, Q., Onda, Y., Takahashi, Y., 2015. Size distribution studies of 137Cs in river water in the Abukuma Riverine system following the Fukushima Dai-ichi Nuclear Power Plant accident. J. Environ. Radioact. 139, 379–389. URL: https://linkinghub.elsevier.com/retrieve/pii/S0265931X14001519 https://doi.org/10.1016/j.jenvrad.2014.05.011.
Sawhney, B.L., 1972. Selective sorption and fixation of cations by clay minerals: a review. Clay Clay Miner. 20, 93–100. URL: https://doi.org/10.1346/CCMN.1972.0200208. https://doi.org/10.1346/CCMN.1972.0200208.
Sellier, V., Navratil, O., Laceby, J.P., Allenbach, M., Lefèvre, I., Evrard, O., 2020. Investigating the use of fallout and geogenic radionuclides as potential tracing properties to quantify the sources of suspended sediment in a mining catchment in New Caledonia, South Pacific. J. Soil. Sediment. 20, 1112–1128. http://link.springer.com/10.1007/s11368-019-02447-8. https://doi.org/10.1007/s11368-019-02447-8.
Steinhauser, G., 2014. Fukushima's forgotten radionuclides: a review of the understudied radioactive emissions. Environ. Sci. Technol. 48, 4649–4663. https://pubs.acs.org/doi/10.1021/es405654c. https://doi.org/10.1021/es405654c.
Stock, B.C., Jackson, A.L., Ward, E.J., Parnell, A.C., Phillips, D.L., Semmens, B.X., 2018. Analyzing mixing systems using a new generation of Bayesian tracer mixing models. PeerJ 6, e5096. https://peerj.com/articles/5096. https://doi.org/10.7717/peerj.5096.
Stock, B.C., Semmens, B.X., Ward, E.J., Parnell, A.C., Phillips, D.L., 2020. MixSIAR: Bayesian Mixing Models in R. URL:. https://doi.org/10.5281/zenodo.1209993.
Stock, B.C., Semmens, B.X., Ward, E.J., Parnell, A.C., Phillips, D.L., 2022. JAGS: Bayesian Mixing Models in RX. URL:. https://doi.org/10.5281/zenodo.1209993.
Taira, Y., Matsuo, M., Yamaguchi, T., Yamada, Y., Orita, M., Takamura, N., 2020. Radiocesium levels in contaminated forests has remained stable, even after heavy rains due to typhoons and localized downpours. Sci. Rep. 10, 19215. https://www.nature.com/articles/s41598-020-75857-1. https://doi.org/10.1038/s41598-020-75857-1.
Tamaoki, M., Yabe, T., Furukawa, J., Watanabe, M., Ikeda, K., Yasutani, I., Nishizawa, T., 2016. Comparison of potentials of higher plants for phytoremediation of radioactive cesium from contaminated soil. Environ. Control Biol. 54, 65–69. URL: https://www.jstage.jst.go.jp/article/ecb/54/1/54_65/_article https://doi.org/10.2525/ecb.54.65.
Taniguchi, K., Onda, Y., Smith, H.G., Blake, W., Yoshimura, K., Yamashiki, Y., Kuramoto, T., Saito, K., 2019. Transport and redistribution of Radiocesium in Fukushima fallout through Rivers. Environ. Sci. Technol. 53, 12339–12347. https://pubs.acs.org/doi/10.1021/acs.est.9b02890. https://doi.org/10.1021/acs.est.9b02890.
Thiry, Y., Albrecht, A., Tanaka, T., 2018. Development and assessment of a simple ecological model (TRIPS) for forests contaminated by radiocesium fallout. J. Environ. Radioact. 190–191, 149–159. URL: https://linkinghub.elsevier.com/retrieve/pii/S0265931X17309499 https://doi.org/10.1016/j.jenvrad.2018.05.009.
Thothong, W., Huon, S., Janeau, J.L., Boonsaner, A., De Rouw, A., Planchon, O., Bardoux, G., Parkpian, P., 2011. Impact of land use change and rainfall on sediment and carbon accumulation in a water reservoir of North Thailand. Agr Ecosyst Environ 140, 521–533. https://linkinghub.elsevier.com/retrieve/pii/S0167880911000442. https://doi.org/10.1016/j.agee.2011.02.006.
Tiecher, T., Caner, L., Minella, J.P.G., dos Santos, D.R., 2015. Combining visible-based-color parameters and geochemical tracers to improve sediment source discrimination and apportionment. Sci. Total Environ. 527–528, 135–149. URL: https://linkinghub.elsevier.com/retrieve/pii/S0048969715300401 https://doi.org/10.1016/j.scitotenv.2015.04.103.
Tsubokura, M., Murakami, M., Takebayashi, Y., Nomura, S., Ono, K., Ozaki, A., Sawano, T., Kobashi, Y., Oikawa, T., 2019. Impact of decontamination on individual radiation doses from external exposure among residents of Minamisoma City after the 2011 Fukushima Daiichi nuclear power plant incident in Japan: a retrospective observational study. J. Radiol. Prot. 39, 854–871. https://iopscience.iop.org/article/10.1088/1361-6498/ab280e. https://doi.org/10.1088/1361-6498/ab280e.
Vandromme, R., Hayashi, S., Tsuji, H., Evrard, O., Grangeon, T., Landemaine, V., Laceby, J.P., Wakiyama, Y., Cerdan, O., 2023. Lessons learnt on the impact of an unprecedented soil decontamination program in Fukushima on contaminant fluxes. Proceedings of the National Academy of Sciences 120, e2301811120. https://pnas.org/doi/10.1073/pnas.2301811120. https://doi.org/10.1073/pnas.2301811120.
Verstraeten, G., Poesen, J., 2000. Estimating trap efficiency of small reservoirs and ponds: methods and implications for the assessment of sediment yield. Prog. Phys. Geogr. Earth Environ. 24, 219–251. http://journals.sagepub.com/doi/10.1177/030913330002400204. https://doi.org/10.1177/030913330002400204.
Wakahara, T., Onda, Y., Kato, H., Sakaguchi, A., Yoshimura, K., 2014. Radiocesium discharge from paddy fields with different initial scrapings for decontamination after the Fukushima Dai-ichi Nuclear Power Plant accident. Environ. Sci.: Processes Impacts 16, 2580–2591. http://xlink.rsc.org/?DOI=C4EM00262H. https://doi.org/10.1039/C4EM00262H.
Walling, D.E., Owens, P.N., Waterfall, B.D., Leeks, G.J., Wass, P.D., 2000. The particle size characteristics of fluvial suspended sediment in the Humber and Tweed catchments, UK. Sci. Total Environ. 251–252, 205–222. URL: https://linkinghub.elsevier.com/retrieve/pii/S0048969700003843 https://doi.org/10.1016/S0048-9697(00)00384-3.
Wetzel, R.G., 2001. Rivers and lakes — their distribution, origins, and forms. In: Limnology. Lake and River Ecosystems, third edition ed. Elsevier, pp. 15–42. URL: https://linkinghub.elsevier.com/retrieve/pii/B9780080574394500071 https://doi.org/10.1016/B978-0-08-057439-4.50007-1.
Whitaker, A.C., Chapasa, S.N., Sagras, C., Theogene, U., Veremu, R., Sugiyama, H., 2022. Estimation of baseflow recession constant and regression of low flow indices in eastern Japan. Hydrol. Sci. J. 67, 191–204. https://www.tandfonline.

com/doi/full/10.1080/02626667.2021.2003368. https://doi.org/10.1080/02626667.2021.2003368.

Yamashiki, Y., Onda, Y., Smith, H.G., Blake, W.H., Wakahara, T., Igarashi, Y., Matsuura, Y., Yoshimura, K., 2014. Initial flux of sediment-associated radiocesium to the ocean from the largest river impacted by Fukushima Daiichi Nuclear Power Plant. Sci. Rep. 4, 3714. URL: https://www.nature.com/articles/srep03714 https://doi.org/10.1038/srep03714.

Yamashita, J., Enomoto, T., Yamada, M., Ono, T., Hanafusa, T., Nagamatsu, T., Sonoda, S., Yamamoto, Y., 2014. Estimation of soil-to-plant transfer factors of radiocesium in 99 wild plant species grown in arable lands 1 year after the Fukushima 1 Nuclear Power Plant accident. J. Plant Res. 127, 11–22. URL: http://link.springer.com/10.1007/s10265-013-0605-z https://doi.org/10.1007/s10265-013-0605-z.

Zuazo, V.H.D., Pleguezuelo, C.R.R., 2009. Soil-erosion and runoff prevention by plant covers: a review. In: Lichtfouse, E., Navarrete, M., Debaeke, P., Véronique, S., Alberola, C. (Eds.), Sustainable Agriculture. Springer, Netherlands, Dordrecht, pp. 785–811. http://link.springer.com/10.1007/978-90-481-2666-8_48. https://doi.org/10.1007/978-90-481-2666-8_48.